

# Dynamically Influenced Molecular Clouds in the Nucleus of NGC 6946: Variations in the CO Isotopic Line Ratios

David S. Meier<sup>1,2</sup> & Jean L. Turner<sup>2,3</sup>

## ABSTRACT

We present high resolution ( $\sim 5''$ ) maps of the  $J = 1 - 0$  transitions of  $^{13}\text{CO}$  and  $\text{C}^{18}\text{O}$  towards the nucleus of NGC 6946, made with the Owens Valley Millimeter Array. The images are compared with existing  $^{12}\text{CO}(1-0)$  maps to investigate localized changes in gas properties across the nucleus. As compared to  $^{12}\text{CO}$ , both  $^{13}\text{CO}$  and  $\text{C}^{18}\text{O}$  are more confined to the central ring of molecular gas associated with the nuclear star formation; that is,  $^{12}\text{CO}$  is stronger relative to  $^{13}\text{CO}$  and  $\text{C}^{18}\text{O}$  away from the nucleus and along the spiral arms. The  $^{12}\text{CO}(1-0)/^{13}\text{CO}(1-0)$  line ratio reaches very high values of  $>40$ . We attribute the relative  $^{13}\text{CO}$  weakness to a rapid change in the interstellar medium from dense star forming cores in a central ring to diffuse, low density molecular gas in and behind the molecular arms. This change is abrupt, occurring in less than a beamsize (90 pc), about the size of a giant molecular cloud. Column densities determined from  $^{13}\text{CO}(1-0)$ ,  $\text{C}^{18}\text{O}(1-0)$ , and 1.4 mm dust continuum all indicate that the standard Galactic conversion factor,  $X_{\text{CO}}$ , overestimates the amount of molecular gas in NGC 6946 by factors of  $\sim 3-5$  towards the central ring and potentially even more so in the diffuse gas away from the central starburst. We suggest that the nuclear bar acts to create coherent regions of molecular clouds with distinct and different physical conditions. The  $^{12}\text{CO}(1-0)/^{13}\text{CO}(1-0)$  line ratio in galactic nuclei can be a signpost of a dynamically evolving ISM.

*Subject headings:* galaxies: individual (NGC 6946) — galaxies: ISM — galaxies: nuclei — galaxies: starburst — radio lines: galaxies

## 1. Introduction

Molecular clouds in galactic centers may differ significantly from the molecular clouds we are familiar with from our own Galactic disk. Characteristics of the nuclear regions of galaxies—strong

---

<sup>1</sup>Department of Astronomy, University of Illinois, 1002. W. Green St., Urbana, IL 61801 email: meierd@astro.uiuc.edu

<sup>2</sup>Department of Physics and Astronomy, UCLA, Los Angeles, CA 90095-1562. email: turner@astro.ucla.edu

<sup>3</sup>Visiting Associate, Department of Astronomy, Caltech, Pasadena CA 91125

tidal forces, rapid rotational timescales, the propensity for molecular cloud interactions due to confined spaces and non-circular motions, the tendency toward extreme star formation events—can easily leave their imprints on the properties of giant molecular clouds (GMCs), and hence star formation.

Some of the first indications that GMCs in starbursts are unusual came with the discovery of bright, high J transitions of CO and the detection of bright HCN(1-0) lines in nearby, actively star-forming nuclei, both indicative of warm, dense gas (eg., Ho, Turner, & Martin 1987; Nguyen-Q-Rieu, Nakai, & Jackson 1989; Carlstrom et al. 1990; Turner, Martin, & Ho 1990; Scoville et al. 1991; Solomon, Downes & Radford 1992; Nguyen-Q-Rieu et al. 1992). In the more extreme starbursts of distant ultraluminous infrared galaxies, CO and HCN observations seem to indicate volume densities of greater than  $10^3 - 10^4 \text{ cm}^{-3}$  over kpc scales (eg. Scoville et al. 1991; Okumura et al. 1991; Downes & Solomon 1998; Solomon, Downes & Radford 1992; Gao & Solomon 2003). The remarkably large amounts of high density gas in these luminous galaxies likely are the cause of their high star formation rates.

Despite the certain presence of *high density* molecular gas, these starbursts are often found to have low  $^{12}\text{CO}(2-1)/^{12}\text{CO}(1-0)$  line ratios (Radford, Downes & Solomon 1991; Papadopoulos & Ivison 2002) and high  $^{12}\text{CO}(1-0)/^{13}\text{CO}(1-0)$  line ratios (Sage & Isbell 1991; Aalto et al. 1991, 1995; Casoli, Dupraz, & Combes 1992; Aalto et al. 1997; Taniguchi & Ohyama 1998; Taniguchi, Ohyama & Sanders 1999), characteristic of *low density* gas. The explanation for this apparent contradiction is not yet clear. Explanations for the anomalously high  $^{12}\text{CO}(1-0)/^{13}\text{CO}(1-0)$  ratios tend to fall into two main categories: unusual physical conditions resulting in low CO opacities or abundance anomalies. If the CO isotopic ratios arise from diffuse, low opacity gas, this might be an indicator of starburst feedback or dynamical cloud dispersal, either of which could result in a diffuse gaseous medium capable of inhibiting future star formation. If instead the explanation for the isotopic ratios is unusual abundances, then the presence of high  $^{12}\text{CO}(1-0)/^{13}\text{CO}(1-0)$  might be a useful indicator of chemical evolution of gas in the presence of star formation.

In distant galaxies distinguishing between these alternatives is difficult because of poor spatial resolution. In nearby galaxies, interferometric imaging at resolutions of a few arcseconds allows us to resolve changes in physical and chemical conditions on the scale of individual GMCs ( $\sim 50 \text{ pc}$ ). Observations of the starbursts in M 82 and IC 342 have demonstrated that small-scale changes in isotopic line ratios are present and correlate with changes in gas properties (e.g., Turner & Hurt 1992; Wright et al. 1993; Neininger et al. 1998; Meier, Turner & Hurt 2000; Weiß et al. 2001; Meier & Turner 2001). In this work, we extend such studies to the nearby, spiral nucleus with active nuclear star formation, NGC 6946.

NGC 6946 is a nearby ( $\sim 5.2 \text{ Mpc}$ ), fairly face-on, barred spiral galaxy (Table 1). One of the brightest galaxies in the mid-infrared sky (Rieke & Lebofsky 1978), NGC 6946 is also bright in CO (Ball et al. 1985; Sofue et al. 1988; Weliachew, Casoli & Combes 1988; Regan & Vogel 1995; Sakamoto et al. 1999) and radio continuum (Turner & Ho 1983). NGC 6946 is currently the site

of a moderate starburst that is 7 - 20 Myrs old (Engelbracht et al. 1996). Belley & Roy (1992) find a flattened abundance gradient over the central 2.5 kpc, suggesting radial mixing of gas has occurred.

Here we compare interferometric  $^{13}\text{CO}(1-0)$  and  $\text{C}^{18}\text{O}(1-0)$  observations to  $^{12}\text{CO}(1-0)$  with two main goals in mind: first to obtain more reliable images of the true molecular column density in the nucleus; and second, to correlate the observed line ratios with other gas properties in order to determine what the isotopic ratios tell us about the structure of the molecular ISM in NGC 6946 and starbursts in general.

## 2. Observations

Aperture synthesis observations of the  $^{13}\text{CO}(1-0)$  and  $\text{C}^{18}\text{O}(1-0)$  lines in NGC 6946 were made with the Owens Valley Radio Observatory (OVRO) Millimeter Interferometer between 1999 September 26 and 1999 November 28. 2.7 mm and 1.4 mm continuum measurements in a separate 1 GHz bandwidth filter were also obtained. The interferometer consists of six 10.4 meter antennas with cryogenically cooled SIS receivers (Padin et al. 1991; Scoville et al. 1994). System temperatures (single sideband) ranged from 180 to 380 K at 2.7 mm. The transitions were observed simultaneously making use of OVRO’s multiple-line spectrometer capabilities, hence share the same instrumental configurations, phase centers, and weather. The instrumental parameters are presented in Table 2.

Data were calibrated using the MMA software package. Phase calibration was done every 25 minutes using the calibrator 2037+511. Absolute flux calibration was done using Neptune for primary flux calibration and 3C273, 3C84 and 3C454.3 as secondary flux calibrators. Due to variability of the quasars, Neptune’s low elevation and imprecise 2.7 mm brightness, the absolute flux calibration is estimated to be good to 10 % for the 2.6 mm data (and 20 % for the 1.4 mm continuum map). The dataset was reduced using the NRAO AIPS data reduction package. The maps are naturally-weighted and primary beam-corrected. In making the zeroth moment (integrated intensity) maps, a mask was generated to help minimize the inclusion of noise into the maps from non-signal portions of these wide lines. The naturally-weighted dataset was smoothed to a resolution of  $10''$ , and all regions below  $2\sigma$  were blanked. This mask was then used on the full resolution dataset to blank out non-signal portions. Only emission greater than  $1.2\sigma$  was included in making the integrated intensity maps. In making the line ratio maps, regions with emission below  $3\sigma$  in either map were blanked to avoid taking ratios of low signal-to-noise emission.

Lack of short baselines limits our sensitivity to structures on scales larger than  $\sim 40''$  at 2.7 mm ( $\sim 20''$  for the 1.4 mm continuum map). To estimate the amount of extended flux the interferometer resolves out of the maps, spectra integrated over the single-dish beamsizes were compared to available single-dish spectra. For NGC 6946, Paglione et al. (2001) obtain an integrated intensity of  $4.8 \text{ K km s}^{-1}$  for  $^{13}\text{CO}(1-0)$  (assuming  $\eta_{mb} = 0.5$  for the FCRAO antenna). Convolution of the interferometer

channel maps to the  $45''$  resolution of the single-dish and sampling the map at the same location yields a line intensity of  $3.0 \text{ K km s}^{-1}$ , or 63 % of the flux. A similar analysis of  $\text{C}^{18}\text{O}(1-0)$  based on a comparison with the  $22''$  resolution spectra of Walsh et al. (2002) suggests that  $\sim 75$  % of the single-dish flux has been detected, consistent with the  $^{13}\text{CO}(1-0)$  value.

$^{12}\text{CO}(1-0)$  data has been kindly provided by S. Ishizuki (Sakamoto et al. 1999) for comparison with the isotopic line data. While the data were taken at the Nobeyama Radio Observatory Millimeter Array (NRO) not OVRO, this difference should not strongly affect the maps since the NRO array is similar in layout to OVRO with similar  $(u, v)$  coverage. Also the Ishizuki  $^{12}\text{CO}(1-0)$  map recovers 76 % of the single-dish flux over the mapped region (Sakamoto et al. 1999), a significant fraction of the total flux and very similar to that found for the isotopomers. Moreover, the similarity of the NRO map and the BIMA  $^{12}\text{CO}(1-0)$  map, which is more sensitive to extended emission (Regan & Vogel 1995; Helfer et al. 2003), demonstrates that the observed distribution is not a strong function of the array used.

To simplify the nomenclature, we use “CO” to denote the main isotopomer,  $^{12}\text{C}^{16}\text{O}$ ,  $^{13}\text{CO}$  to denote “ $^{13}\text{C}^{16}\text{O}$ ”; and  $\text{C}^{18}\text{O}$  to denote “ $^{12}\text{C}^{18}\text{O}$ ”. The ratio of integrated line intensities,  $\int T_{\text{CO}(1-0)} dv / \int T_{^{13}\text{CO}(1-0)} dv$  and  $\int T_{\text{CO}(1-0)} dv / \int T_{\text{C}^{18}\text{O}(1-0)} dv$  are represented by  $R_{13}$  and  $R_{18}$ , respectively. Since we observed the 3 mm  $J=1-0$  transitions,  $J$  values are omitted unless different from  $J=1-0$ , or where omitting results in ambiguity.

### 3. Results

#### 3.1. Morphology and Kinematics of the CO Emitting Gas

The  $^{13}\text{CO}$  channel maps for NGC 6946 are presented in Figure 1. Peak antenna temperatures obtained from the  $^{13}\text{CO}$  channels are  $\sim 0.82 \text{ K}$ . Emission is present in channels from  $V_{\text{LSR}} = -43 \text{ km s}^{-1}$  to  $164 \text{ km s}^{-1}$ . Redshifted velocities are towards the southwest. No significant differences between CO and  $^{13}\text{CO}$  velocity dispersions or systemic velocities are seen. The morphology and kinematics (not shown) of  $\text{C}^{18}\text{O}$ , though limited by faintness, are consistent with the  $^{13}\text{CO}$  data. Integrated intensity maps of the three CO isotopomers are presented to the same resolution and scale in Figure 2. Integrated intensities of each transition are listed in Table 3 for the locations of the GMCs.

The CO emission within the central 1.3 kpc ( $50''$ ) of NGC 6946 is spatially asymmetric (Regan & Vogel 1995; Sakamoto et al. 1999). The CO integrated intensity peaks at the starburst, and remains relatively bright along the northern arm. The southern arm is weaker. The optical spiral structure of NGC 6946 also reflects this asymmetry, although on a much larger scale, with a “heavy” northern arm (Arp 1966).

By contrast,  $^{13}\text{CO}$  emission is more symmetric and spatially confined to the center of the galaxy than is CO. The  $^{13}\text{CO}$  emission is suggestive of a central disk-like structure with the starburst

occurring at the southwestern edge of the disk. A secondary peak in CO at the northern end of the molecular bar is also bright in  $^{13}\text{CO}$ . Lower resolution studies of the CO showed extended bar-like CO and hints of non-circular motion suggesting that it is a true bar (eg. Sofue et al. 1988; Ishizuki et al. 1990b). From their high resolution CO map, Regan & Vogel (1995) argued that it is difficult to distinguish between a nuclear bar and a continuation of spiral arms, based on morphology alone. Elmegreen, Chromey & Santos (1998) suggested the possibility of nested bars in NGC 6946.

In Table 1, we have listed the near-IR centroid of NGC 6946 as measured from 2MASS J, H, and K images. The peak 2 cm continuum emission (Tsai et al. 2004, in preparation) is located  $\sim 1''$  ENE of the near-IR center, although this emission is extended. The dynamical center is, within the uncertainties, coincident with the near-IR peak, as one might expect if the near-IR emission traces the mass. Whereas the  $^{13}\text{CO}$  peak is  $\sim 2''$  ESE of the near-IR peak.

To study the impact of the galactic potential on the molecular gas, we first investigate the kinematics of the nucleus. We use two methods to study the velocity field in NGC 6946. One, we fit the entire velocity field to a disk in circular rotation and use this to determine the azimuthally averaged rotation curve of the central region (Figure 3a). Secondly, position-velocity (PV) diagrams are constructed along the major and minor axes (Figure 4). The major axis PV diagram should essentially traced out the same shape as the rotation curve (reflected through the origin), but it also provides additional information on the distribution of emission versus velocity. Comparison of the major axis PV diagram in Figure 4b with the rotation curve of Figure 3a demonstrates this is true. The rotation curve increases steeply for  $\sim 7.5''$  then turns over and falls for  $\sim 5''$  before it reverses and continues to rise out to larger distances. The radius of turnover corresponds to the edge of the central ring. The same structure can be seen in the PV diagram. In Figure 4b, the two emission peaks on either side of the center of the major axis PV diagram hint that the disk-like structure seen in the isotopomers does not extend all the way to the center of the galaxy and hence is ring-like (compare Figure 4b with Figure 5 of Sakamoto et al. 1999). The central ring-like structure may reflect the  $x_2$  orbits of an inner Lindblad Resonance (ILR) or possibly gas response to the small inner bar.

In the case of pure circular motion the PV diagram taken along the minor axis predicts emission only at zero velocity, since all motion would be in the plane of the sky at these locations. Deviations from this imply radial motions are present. In Figure 4c, a large percentage of the emission over the central  $5''$  radius is blueshifted on the SE side of the galaxy, and redshifted on the NW side of the galaxy. Since the northern molecular arm is the near one (Elmegreen, Chromey & Santos 1998; Regan 2000), consistent with trailing spiral arms, these shifts imply that the gas is orbiting radially inward from both sides. Radial velocities peak at  $|v_r| \sim 80 \text{ km s}^{-1}$  at the center, decreasing as one moves away from the center of the galaxy. Strong radial motion is not obvious beyond a radius of  $\sim 7''$ . Either the gas inflow strengthens as the nucleus is approached, or more likely the gas streamlines are turning progressively more radial with decreasing galactocentric distance.

The overall kinematics of NGC 6946's nucleus can be explained either as non-circular motions

in response to a barred potential, or as a region of enhanced mass density in the nucleus. In the case of a barred potential, non-circular motions “contaminate” the rotation curve causing the observed rotation curve to develop breaks (eg. Sakamoto et al. 1999). Radial inflow will raise the inferred circular velocities. If the radial flow dominates over a narrow radii around the molecular ring, the velocity peak at  $\sim 7''$  is explained. Therefore the non-circular motion associated with a barred potential provides a good explanation for both the radial motions seen in the minor axis PV diagram and the turnover in the rotation curve.

Alternatively, the rotation curve could be due to a compact nuclear mass distribution. This would affect the dynamics and the location of orbital resonances. In Figure 3a-b, the rotation curve of NGC 6946 is shown fit with a 2-component mass density distribution: one with a characteristic scale of 275 pc ( $11''$ ) and a peak velocity of  $175 \text{ km s}^{-1}$ , roughly consistent with the size of the secondary nuclear bar (Elmegreen, Chromey & Santos 1998), and the other with a scale of 5 kpc ( $200''$ ) that reaches the same peak velocity. This 2-component mass distribution matches the observed velocity profile. If we (somewhat arbitrarily) assume the density wave pattern speed determined for the large scale disk (Crosthwaite et. al. 2004, in preparation) of  $\omega_p \simeq 66 \text{ km s}^{-1} \text{ kpc}^{-1}$ , is the same for both, the “buckle” in the nuclear rotation curve corresponds to an inner ILR near the ring, at a radius of  $7.5''$ , and the location of the clumps at the ends of the molecular bar would correspond to an outer ILR, at a radius of  $26''$ .

Given the strong non-circular motions across the nuclear region, we favor a barred potential over a central mass for explaining the gas morphology and kinematics.

### 3.2. Properties of the Nuclear GMCs in NGC 6946

Giant molecular clouds (GMCs) in NGC 6946 are identified from the  $^{13}\text{CO}$  data. The method of localizing and fitting the GMCs is the same as given in Meier & Turner (2001). Results are given in Table 4 and Figure 4a. Given a distance of 5.2 Mpc ( $1'' \simeq 25 \text{ pc}$ ), only the larger GMCs are spatially resolvable (fitted sizes  $> 1/2$  the FWHM of the beamsizes). GMCs that are off the central ring region (A, C, D, H, G) are the most isolated and hence their fits are the most robust. GMCs away from the central ring generally have deconvolved sizes  $\sim 50 - 100 \text{ pc}$  in size, FWHM linewidths of  $25 - 40 \text{ km s}^{-1}$  and predicted virial masses of  $\gtrsim 10^7 M_\odot$ . The central ring GMCs have implied virial masses of  $\sim 10^8 M_\odot$ ; however, while NGC 6946 is not highly inclined ( $i = 40^\circ$ ), the GMCs that are centered along the central ring almost certainly have linewidths contaminated by the steep rotational velocity gradient and non-circular motions present. The derived virial masses are consistent with the enclosed dynamical masses (§4.2).

### 3.3. The High and Variable Isotopic CO Line Ratios in NGC 6946

Figure 5 (and Table 5) shows the  $R_{13}$  and  $R_{18}$  isotopic line ratio maps for the nucleus of NGC 6946. Two unusual characteristics of the line ratios are evident: there are regions with very high values compared to the Galaxy, and the ratios vary rapidly across the nuclear region. Over the mapped regions,  $R_{13}$  reaches values greater than 25 along the northern arm. By comparison, Galactic disk molecular clouds generally have values of 6 - 7 (Polk et al. 1988). In almost all cases,  $^{13}\text{CO}$  ( $\text{C}^{18}\text{O}$  for  $R_{18}$ ) limits the region covered by the ratio map, which implies that blanked regions in Figure 5 have even higher  $R_{13}$ , with values as high as 60 estimated for in these blanked regions. The lower values of  $R_{13}$  are  $\sim 10$  near the starburst, more consistent with what is typically seen in starburst nuclei (eg., Aalto et al. 1991, 1995). The lowest isotopic line ratios ( $R_{13} \simeq 4 - 5$ ) are found  $\sim 5''$  east of the main starburst, extending perpendicular to the main CO arms. Along the northern arm gas transitions from its lowest values of  $R_{13}$  to  $R_{13} \gtrsim 25$  in one beamwidth ( $\lesssim 100$  pc). The transition from  $R_{13} \sim 10$  regions dominating towards the starburst to  $R_{13} \gtrsim 25$  is even sharper, being unresolved by our beam. Evidently, just outside the central ring the molecular gas undergoes a sharp change in gas physical conditions.

To test if the high isotopic ratio could be due to a larger amount of flux resolved out of the  $^{13}\text{CO}$  transition versus the CO, we have taken 26 % of the total CO flux (the percentage of the flux resolved out at CO) and distributed it uniformly over the central  $30'' \times 60''$ , and 38 % of the  $^{13}\text{CO}$  and distributed it uniformly over the same region, and then recalculated  $R_{13}$ . This approximates what we would expect to see if the flux resolved out of each map were distributed uniformly over the largest spatial scales. The newly calculated  $2\sigma$  lower limit to  $R_{13}$  at the arm locations become  $>47$ . Therefore, the very high ratios in the arm region cannot be due to differentially resolved-out flux.. Similar results are seen in  $R_{18}$ , when taking account its more limited coverage, providing further evidence for true changes in gas physical conditions and not just anomalies in  $^{13}\text{CO}$ . Typical values of the  $^{13}\text{CO}/\text{C}^{18}\text{O}$  line ratio towards the high S/N regions is  $\sim 2.5$ .

Comparisons with interferometric HCN(1-0) data show that, within the uncertainties, the morphology of the  $^{13}\text{CO}$  and  $\text{C}^{18}\text{O}$  transitions match closely what is seen in the HCN(1-0) (Helfer & Blitz 1997). The HCN/CO ratio map of Helfer & Blitz (1997) correlates well with the inner structure of  $R_{13}$ . Both show a “saddle” shaped distributed approximately perpendicular to the CO arms (Helfer & Blitz 1997). This suggests that density changes sensitively influence the isotopic line intensities.

### 3.4. Millimeter Continuum from Star Forming HII Regions in NGC 6946

Displayed in Figure 6 are the 2.7 mm continuum map of NGC 6946 overlaid on the HST  $\text{Pa}\alpha$  image (Böker et al. 1999), convolved to the same beamsize as the OVRO maps, and the 1.4 mm continuum map overlaid on the  $^{13}\text{CO}(1-0)$  integrated intensity map. 2.7 mm continuum is reliably detected at only one location,  $1.8''$  NNW of GMC E1. Its position is within  $1''$  of the 2 cm

continuum peak (Tsai et al. 2004, in preparation). A Gaussian fit shows that the 2.7 mm source is slightly resolved with a size of  $7'' \times 2''$  ( $PA \simeq 120^\circ$ ), and a total flux of  $S_{2.7mm} = 8.3 \pm 1.0$  mJy. The full resolution HST  $P\alpha$  image, which is sensitive to weaker star formation than the millimeter continuum, also shows a secondary star forming peak just east of the starburst, at the secondary HCN peak and the  $R_{13}$  minima, and also faint HII regions encircling the entire central ring (Böker et al. 1999). The total flux detected at 2 cm is 23 mJy (Turner & Ho 1983). The spectral index between 2 cm and 2.7 mm is  $\alpha_{2.7}^2 \simeq -0.51 \pm 0.07$ . Hence, the starburst is a mixture of bremsstrahlung and synchrotron at 2 cm, which is consistent with the 6 - 2 cm spectral index (Turner & Ho 1983) and the distribution of compact sources (Tsai et al. 2004, in preparation).

Continuum emission is also detected at 1.4 mm towards GMC E1. The source at 1.4 mm has a size similar to that found at 2.7 mm. The total flux at 1.4 mm is  $21 \pm 4$  mJy. The 2.7 - 1.4 mm spectral index implied by this flux is  $\alpha_{1.4}^{2.7} = +1.4 \pm 0.5$ . The rising spectral index suggests that dust emission begins to contribute at 1.4 mm. Assuming for simplicity that all of the 2.7 mm flux is a mixture of thermal free-free emission with a spectral index of  $\alpha = -0.1$  and dust emission with a spectral index of  $\alpha = +3.5$  (slightly overestimates the free-free emission since some 2.7 mm may still be synchrotron), we derive free-free fluxes of  $\sim 7.0$  mJy at 2.7, and  $\sim 6.5$  mJy at 1.4 mm, and dust fluxes of 1.2 mJy at 2.7 mm, and  $14 \pm 5$  mJy at 1.4 mm. The dust flux is confined within the  $\sim 6''$  associated with GMC E1. The molecular mass implied by the dust emission is discussed in section 4.2.

Using the 2.7 mm continuum to constrain the number of ionizing photons, (and hence massive stars), a Lyman continuum rate of  $N_{Lyc} = 2.1 \pm 0.2 \times 10^{52} \text{ s}^{-1}$ , or 2800 “effective” O7V stars is obtained (assuming  $T_e = 8000 \text{ K}$ ; eg. Mezger & Henderson 1967; Vacca, Garmany & Shull 1996). This is a factor of two higher than is estimated from  $\text{Br}\gamma$  data by Engelbracht et al. (1996). High extinction is probably the explanation for the difference, given the  $\text{H}_2$  column densities are at least  $\sim 1 - 3 \times 10^{22} \text{ cm}^{-2}$  ( $A_V \sim 6 - 17$ ; Table 6).

## 4. Discussion

### 4.1. Physical Conditions of the Molecular Clouds in NGC 6946

To relate the observed intensities and line ratios to physical properties of the clouds,  $n_{\text{H}_2}$  and  $T_k$ , a sample of Large Velocity Gradient (LVG) radiative transfer models were run (eg., Goldreich & Kwan 1974; Scoville & Solomon 1974; de Jong, Dalgarno, & Chu 1975). For very opaque lines, LVG models can be unreliable, but for the lower opacity  $^{13}\text{CO}$  and  $\text{C}^{18}\text{O}$  transitions LVG models are expected to yield reasonable results. The LVG model used is the same basic model discussed in Meier, Turner & Hurt (2000), expanded to cover  $n_{\text{H}_2} = 10^1 - 10^6 \text{ cm}^{-3}$ ,  $T_k = 1.5 - 150 \text{ K}$ , and  $X_{\text{CO}}/dv/dr = 10^{-3} - 10^{-7.7}$ . A  $[\text{CO}/\text{H}_2]$  abundance of  $8.5 \times 10^{-5}$  (Frerking et al. 1982) and a velocity gradient of  $3 \text{ km s}^{-1} \text{ pc}^{-1}$  was adopted as the standard case. A wide range of  $^{13}\text{CO}$  and  $\text{C}^{18}\text{O}$  relative abundances and velocity gradients were tested. Figure 7a displays the results



assuming  $[\text{CO}/^{13}\text{CO}] \simeq 40$  and  $[\text{CO}/\text{C}^{18}\text{O}] \simeq 150$ , typical values for starburst nuclei (Henkel & Mauersberger 1993; Wilson & Rood 1994; Wilson 1999). Only ratios are used to constrain parameter space, so the derived solutions are independent of filling factors, as long as they are the same for both transitions.

In addition to the CO LVG models, a set of HCN LVG models were run. The first 12 J transitions were included since collision coefficients are available only for those (Green & Thaddeus 1974). We do not extend the models to densities larger than  $10^5 \text{ cm}^{-3}$  to avoid significant populations in  $J_{\text{max}}$ ; our derived densities are lower than this anyway. An HCN abundance,  $[\text{HCN}/\text{H}_2] = 1.5 \times 10^{-8}$ , consistent with galactic HCN abundances (eg., Irvine, Goldsmith, & Hjalmarson 1987; Paglione et al. 1998), and a velocity gradient of  $3 \text{ km s}^{-1} \text{ pc}^{-1}$  was assumed. From the observed ratios  $R_{13}$ ,  $R_{18}$  and  $^{13}\text{CO}/\text{HCN}$ , physical conditions for the starburst region, E1, were estimated.

Since both the  $^{13}\text{CO}$  and  $\text{C}^{18}\text{O}$  lines are optically thin (§4.2)  $R_{13}$  and  $R_{18}$  should provide similar constraints on gas density,  $n_{\text{H}_2}$ , and kinetic temperature,  $T_K$ , with any differences ascribed to inaccuracies in the adopted  $[^{13}\text{CO}/\text{C}^{18}\text{O}]$  abundance ratio. Both  $R_{13}$  and  $R_{18}$  predict  $n_{\text{H}_2} \sim 10^{2.5-3} \text{ cm}^{-2}$  and  $T_k \sim 10 - 40 \text{ K}$  ranging to  $n_{\text{H}_2} \sim 10^{4.5} \text{ cm}^{-2}$  and  $T_k \sim 100 - 150 \text{ K}$ .  $R_{13}$  predicts a slightly lower range in  $n_{\text{H}_2}$ ,  $T_K$  than does  $R_{18}$ . This suggests that the adopted  $[^{13}\text{CO}/\text{C}^{18}\text{O}]$  abundance ratio is slightly overestimated. The solution ranges agree if the  $[^{13}\text{CO}/\text{C}^{18}\text{O}]$  abundance ratio is lowered from 3.75 (150/40) to  $\sim 2.5$  (150/60).

Further constraints on  $n_{\text{H}_2}$  and  $T_K$  can be obtained by adding the  $^{13}\text{CO}/\text{HCN}$  line ratio, from HCN observations of Helfer & Blitz (1997) at a nearly identical beamsize. Towards GMC E1,  $^{13}\text{CO}/\text{HCN} \simeq 1.0 \pm 0.2$ . The similarity in intensity of the  $^{13}\text{CO}$  and HCN lines immediately argue for high densities ( $n_{\text{H}_2} \gtrsim 10^{4.5}$ ) as required to thermalize HCN. The best fit, including HCN, is  $n_{\text{H}_2} \sim 10^{4.2} \text{ cm}^{-3}$  and  $T_k \sim 90 \text{ K}$ . The single-dish value of a characteristic  $\Delta J$  line ratio,  $\text{CO}(3-2)/\text{CO}(1-0)$  is  $0.71 \pm 0.2$  (Walsh et al. 2002). Using this line ratio with  $R_{13}$  or  $R_{18}$  favors  $n_{\text{H}_2} \sim 10^3 \text{ cm}^{-3}$  and  $T_k \sim 30 \text{ K}$ , consistent with the  $n_{\text{H}_2} \sim 10^{3.4} \text{ cm}^{-3}$ ,  $T_k \sim 40 \text{ K}$  obtained by Walsh et al. (2002). The fact that the high resolution interferometer data towards the starburst favors warmer, denser solutions than those obtained from single-dish data suggests that the molecular clouds are cooler and less dense outside the central starbursting ring and that this lower excitation, diffuse molecular component dilutes the single-dish ratios.

In the case of the high  $R_{13}$  ratio arm regions, for  $[\text{CO}/^{13}\text{CO}] = 40$  and  $R_{13} > 40$ , no portion of parameter space in the standard model is acceptable. Assuming LVG is applicable, we are forced to conclude that the  $^{13}\text{CO}$  relative abundance is lower than the assumed value of  $[\text{CO}/^{13}\text{CO}] = 40$ , and densities are  $n_{\text{H}_2} \lesssim 10^2 \text{ cm}^{-3}$ . At these low densities  $^{13}\text{CO}$  emission is strongly subthermal, and  $R_{13}$  and  $R_{18}$  are approximately independent of  $T_K$ . These constraints can be loosened somewhat by raising  $X_{\text{CO}}/dv/dr$  significantly (Figure 7b), but it is unclear how the velocity gradients could be stronger along the arms than in the high linewidth, central ring region (Table 4). Single-dish observations of the higher J transitions  $\text{CO}(2-1)/\text{CO}(1-0)$ ,  $\text{CO}(3-2)/\text{CO}(2-1)$  and  $\text{CO}(4-3)/\text{CO}(3-2)$  line ratios all decrease up the northern arm (Wall et al. 1993; Nieten et al. 1999; Israel & Baas

2001; Walsh et al. 2002). While not extremely low, these ratios do suggest that even the higher opacity (less subthermal) CO transitions may not be highly excited.

In summary, the LVG solutions for  $n_{H_2}$  and  $T_K$  based on single-dish ratios ( $\sim 22''$  beam) are lower than our interferometer solutions because the large single-dish beamsizes averages the low density, lower temperature spiral arm gas with the warmer, denser molecular gas associated with the starburst. The bright, compact starburst gas dominates the interferometer maps. On the basis of the incompatibility of the line ratios with the CO line intensity, it has been argued that the nuclear ISM in NGC 6946 requires at least two distinct components with distinct physical conditions (Paglione et al. 2001; Israel & Baas 2001). Our interferometer images confirm this conclusion, and resolves the spatial distribution of each component.

#### 4.2. CO as a Tracer of Molecular Gas Mass: The Conversion Factor in the Nucleus of NGC 6946

One might expect that the unusual and varying cloud conditions in NGC 6946’s nucleus will have an affect the CO conversion factor,  $X_{CO}$ , which is based on Galactic clouds that have relatively uniform properties. Therefore we consider in detail an estimate of the conversion factor suitable to the nucleus of NGC 6946. To obtain a robust estimate of the amount of molecular gas, column densities derived from the optically thick CO integrated intensity and  $X_{CO}$  are compared with four independent estimates of the column density: from the optically thin  $^{13}CO$  and  $C^{18}O$  lines, from the virial theorem, and from dust.

Table 6 records the column densities derived from CO and a Galactic conversion factor of  $X_{CO} = 2.0 \times 10^{20} \text{ cm}^{-2} (K \text{ km s}^{-1})^{-1}$  (Strong et al. 1988; Hunter et al. 1997). Column densities are derived from the isotopomers using:

$$N(H_2)_{iCO} = 2.42 \times 10^{14} \text{ cm}^{-2} \frac{[H_2]}{[iCO]} \frac{e^{\frac{iE_u}{T_{ex}}}}{(e^{\frac{iE_u}{T_{ex}}} - 1)} I_{iCO} (K \text{ km s}^{-1}), \quad (1)$$

where  $iE_u$  is 5.29 K (5.27 K) for  $^{13}CO$  ( $C^{18}O$ ), and abundances listed in Table 6. Excitation temperatures of  $^{13}T_{ex} = 20$  K and  $^{18}T_{ex} = 10$  K were adopted, taking into account the fact that the isotopomers are likely increasingly subthermal at the relevant densities (§4.1). Derived column densities vary approximately linearly with the chosen  $T_{ex}$ , so uncertainties in  $N_{H_2}$  scale with  $T_{ex}$ . Non-LTE effects such as temperature gradients may explain some portion of the high observed  $R_{13}$  ratio (eg., Meier, Turner & Hurt 2000), although we doubt the opacities are high enough here (see below). Taking into account uncertainties in  $T_{ex}$  and abundances, we expect that column densities of  $N_{H_2}$  derived from isotopomers are accurate to about a factor of two.

For molecular clouds with density profiles given by  $\rho \propto R^{-1}$ , the virial mass is:  $M_v = 189 (\Delta v_{1/2} \text{ km s}^{-1})^2 (R/pc)$ , (eg., MacLaren, Richardson & Wolfendale 1988), where  $R$  is the radius of the cloud, and  $\Delta v_{1/2}$  is the FWHM of the linewidth (following Meier & Turner 2001). The

radius of the clouds is assumed to be  $0.7\sqrt{ab}$ , where  $a$  and  $b$  are the FWHM fitted sizes of the major and minor axes. Virial cloud masses are displayed in Table 6. Virial masses are always much larger than those found by any other method, even for GMCs far away from the central high linewidth molecular ring. In general, the virial estimates of column densities are much greater even than the column densities estimated from CO (e.g., Meier & Turner 2001). This confirms that GMC linewidths are not virial across the nucleus and are dominated by rotational and non-circular motion.

For clouds that are entirely molecular and have a constant gas-to-dust ratio of 100 by mass, the gas mass is related to the 1.4 mm dust continuum flux by (eg., Hildebrand 1983):

$$M_{gas}(1.4 \text{ mm}) = 310 M_{\odot} \left( \frac{S_{1.4mm}}{mJy} \right) \left( \frac{D}{Mpc} \right)^2 \left( \frac{\kappa_{\nu}}{cm^2 g^{-1}} \right)^{-1} \left( e^{\frac{10.56}{T_d}} - 1 \right), \quad (2)$$

where  $\kappa_{\nu}$  is the dust absorption coefficient at this frequency,  $S_{1mm}$  is the 1.4 mm flux,  $D$  is the distance and  $T_d$  is the dust temperature.  $T_d = 40$  K is assumed for the nucleus of NGC 6946 (Engargiola 1991), although the  $T_d$  suitable for the 1.4 mm emission could be lower. The dust opacity,  $\kappa_{\nu}$ , at 220 GHz is taken to be  $3 \times 10^{-3} \text{ cm}^2 \text{ g}^{-1}$ , but is uncertain to a factor of four (Pollack et al. 1994). Dust masses determined from millimeter continuum are only linearly dependent on  $T_d$ , so dust opacity dominates the uncertainty in the mass. The derived total molecular gas mass of GMC E1 based on its dust emission, is  $M_d(M_{\odot}) \simeq 1.2 \pm 0.4 \times 10^7 M_{\odot}$ . The mass is consistent with the  $^{13}\text{CO}$  mass. If one instead uses the dust extinction towards the starburst derived from the NIR,  $A_V \gtrsim 10.4$  (Engelbracht et al. 1996), assumes the starburst is in the center of the GMC, and applies the Galactic conversion between  $N(\text{H}_2)$  and  $A_v$  (Bohlin, Savage & Drake 1978), a column density of  $N_{H_2} \sim 2 \times 10^{22} \text{ cm}^{-2}$  is estimated, within a factor of 50 % of the value obtained from  $^{13}\text{CO}$ .

Column densities obtained from  $^{13}\text{CO}$  and  $\text{C}^{18}\text{O}$  are lower than what is implied by CO: values estimated from  $^{13}\text{CO}$  are low by a factor of  $5 \pm 2$ , and those from  $\text{C}^{18}\text{O}$  are low by a factor of  $3 \pm 2$ . The agreement between the  $^{13}\text{CO}$  and  $\text{C}^{18}\text{O}$  masses is generally good in the high signal-to-noise regions, with the exception of E2. The slight difference between the magnitude of  $X_{CO}$  between  $^{13}\text{CO}$  and  $\text{C}^{18}\text{O}$  can be explained in one of two ways. Either  $^{13}\text{CO}$  is optically thick, with opacities,  $^{13}\tau \sim 5/3$ , or that the relative isotopic abundances that we have assumed are incorrect (§4.1). It is unlikely that the isotopomers are optically thick: even at E1, an opacity of  $^{13}\tau \sim 0.1$  is estimated given the observed linewidth; along the northern arm, even CO may not be very optically thick in this region (assuming CO is optically thin one obtains column densities less than a factor of two higher than the  $^{13}\text{CO}$  value). The more likely explanation is that the relative abundance ratio is incorrect. Given that  $^{13}\text{CO}$  and  $\text{C}^{18}\text{O}$  are optically thin, the  $^{13}\text{CO}/\text{C}^{18}\text{O}$  line ratio should be close to the  $[^{13}\text{CO}/\text{C}^{18}\text{O}]$  abundance ratio. Adopting an average  $^{13}\text{CO}/\text{C}^{18}\text{O}$  line ratios of  $\sim 2.5$ , and a  $[\text{CO}/\text{C}^{18}\text{O}] = 150$ , the favored  $[\text{CO}/^{13}\text{CO}]$  abundance is  $\simeq 60$ .

The  $\text{CO}/^{13}\text{CO}$  abundance ratio in NGC 6946 would have to be  $\sim 200$ , and  $\text{CO}/\text{C}^{18}\text{O} \sim 750$  to make the isotopomer masses consistent with values derived from the Galactic  $X_{CO}$ . While it is

possible that towards the starburst the excitation temperature is underestimated, a very high  $T_{\text{ex}}$  of 40 - 80 K is required to match the Galactic  $X_{\text{CO}}$ . In both cases, these are much higher  $\sim 50$  pc averages than seen anywhere in the Galaxy. Moreover, the dust masses agree with the values obtained from the isotopomers toward the detected GMC, E1, also favoring a lower conversion factor. Regan (2000) has undertaken a detailed, multicolor NIR extinction study of several galaxies including NGC 6946 and derives conversion factors of  $^{6946}X_{\text{CO}} \simeq 0.2 \times 10^{20} \text{ cm}^{-2} (\text{K km s}^{-1})^{-1}$  at the northern arm and  $0.5 \times 10^{20} \text{ cm}^{-2} (\text{K km s}^{-1})^{-1}$  for the central ring area. The analysis here confirms the low  $X_{\text{CO}}$  found by the Regan (2000) study, and suggests that the northern arm, in particular, is relatively overluminous in CO for its column density and mass.

In summary, though the uncertainties are still large due to the weakness of the isotope emission in NGC 6946,  $^{6946}X_{\text{CO}} \simeq 0.5 \times 10^{20} \text{ cm}^{-2} (\text{K km s}^{-1})^{-1}$  for the central 300 pc, possibly dropping another factor of a few away from the central region along the northern arm. This is at least a factor of four smaller than  $X_{\text{CO}}$  in the Galaxy, and is consistent with other findings of low  $X_{\text{CO}}$  in the centers of our own and other galaxies (eg., Dahmen et al. 1998; Regan 2000; Meier & Turner 2001).

#### 4.3. The Mass of $\text{H}_2$ Gas and Efficiency of the Starburst in NGC 6946

Over the central 130 pc ( $6''$ ) of the NGC 6946 the total molecular mass estimated from  $^{13}\text{CO}$  is  $2.8 \times 10^7 M_{\odot}$ , lower than previous estimates using the Galactic conversion factor. The dynamical mass over the same region (Figure 3b) is  $M_{\text{dyn}} = 5.1 \times 10^8 M_{\odot}$ . This implies a molecular mass fraction of  $\sim 5\%$ . The kinematics of the molecular gas in the nuclear region must be governed by the underlying stellar mass distribution.

We can estimate the current star formation efficiency, SFE, based on the gas mass and a stellar mass from the young star formation associated with the millimeter continuum emission. Adopting a ZAMS Salpeter IMF with an upper mass cutoff of  $100 M_{\odot}$  and a lower mass cutoff of  $1 M_{\odot}$ , the total mass of newly formed stars derived from the observed  $N_{\text{Lyc}}$  rate (§3.4) is  $M_* \simeq 4 \times 10^5 M_{\odot}$ , and up to  $10^6 M_{\odot}$  if the IMF goes down to M stars. Therefore, the  $\text{SFE} = M_*/(M_* + M_{\text{gas}})$  is  $\lesssim 3\%$ . This is typical of what is seen in Galactic disk GMCs on similar sizescales (eg., Myers et al. 1986; Leisawitz, Bash, & Thaddeus 1989; Kim & Koo 2003). Evidently, star formation in the nucleus of NGC 6946 is not exceptional in efficiency, only being as intense as it is because of the large amount molecular gas present.

Often star formation is said to result from gravitational disk instabilities, typically characterized by the Toomre  $Q$  parameter (eg. Kennicutt 1989). In the nucleus of NGC 6946,  $Q$  is always much larger than one even if the Galactic conversion factor is assumed, due primarily to the large linewidth (Figure 3d). Star formation traced by the 2.7 mm continuum peaks towards the gas column density peaks traced by  $^{13}\text{CO}$ , but the 2.7 mm continuum only samples the brightest HII regions. However, star formation traced by  $\text{P}\alpha$  also closely correlates with the  $^{13}\text{CO}$ , more so than

with CO. This argues that star formation is more closely correlated with gas surface density, than the ratio of gas surface density to critical surface density ( $Q$ ). In reality, it is likely that the star formation actually correlates with *density* than surface density (differs just by a multiplicative factor if the line of sight dimension is approximately constant), since the isotopomer peaks represent density peaks (§4.1) and, in general, far-IR fluxes are more tightly correlated with HCN than they are with CO (Gao & Solomon 2003).

#### 4.4. Causes of High $R_{13}$ in NGC 6946: Low Density and CO and $C^{18}O$ Abundance Enhancements

A number of possible explanations for the simultaneously very bright CO and weak  $^{13}CO$  has been suggested in the literature, primarily in the context of strong starbursts associated with distant mergers. Two main classes of possibilities are envisioned for generating high  $R_{13}$  ratios in NGC 6946. A first class of possibilities requires unusual isotopic abundances. This might occur through the inflow of metal poor disk gas from the outer disk, isotope-selective fractionation or photodissociation, or chemical evolution due to pollution from in situ nuclear star formation (Casoli, Dupraz, & Combes 1992; Henkel & Mauersberger 1993; Taniguchi & Ohyama 1998; Taniguchi, Ohyama & Sanders 1999). The second class of possibilities involve changes in physical conditions of the molecular gas which lower the CO opacity. This could be caused by, unusually high average gas temperatures, unusually low average gas densities, or unusually high cloud velocity dispersions (Aalto et al. 1991, 1995; Glenn & Hunter 2001; Paglione et al. 2001). Previous work has been limited by lack of spatial resolution, and it is clear from these ratio maps that the cloud properties vary rapidly across the nucleus. The high spatial resolution ( $\lesssim 100$  pc) of these images (and also IC 342: Meier, Turner & Hurt 2000; Meier & Turner 2001) and this nearby galaxy allow for a clearer understanding of what molecular traits are most closely connected to the high  $R_{13}$  gas.

##### 4.4.1. High $R_{13}$ from Opacity Effects

We first discuss models which account for the anomalously high  $R_{13}$  with changes in line opacity due to variations in physical conditions, such as  $n_{H_2}$ ,  $T_K$ , or velocity dispersion. The most direct way to raise  $R_{13}$  (or  $R_{18}$ ) is to decrease the opacity of each line. The first way to do this is to raise  $T_K$ . As  $T_K$  increases the optically thinner low  $J$  transitions of  $^{13}CO$  (and  $C^{18}O$ ) depopulate, lowering their opacities and brightness temperatures, while the brightness temperature of the optically thick CO line increases. So long as the  $^{13}CO$  opacity is not greater than unity,  $R_{13}$  will increase as  $T_K$  increases. In NGC 6946 this is probably not the primary mechanism for enhanced  $R_{13}$  since the regions with the highest  $R_{13}$  are not found near the starforming regions, where the gas should be warmest (Figure 8a). However, changes in  $T_K$  cannot be ruled out completely until the gas temperature distribution is determined from high-resolution, multi-line analysis.

A second way of lowering the opacity of the molecular gas is dynamical. Broadening the linewidth of the molecular gas spreads the total column density over a larger linewidth, reducing the opacity at a given velocity, hence raising  $R_{13}$  (Aalto et al. 1995). It is clear from Figure 8b that there is no correlation between  $R_{13}$  and  $\Delta v$  locally in NGC 6946. In fact, the locations of the highest linewidth are found towards the central ring, but these areas tend to have the lowest  $R_{13}$  (Table 5). Moreover, if in general changes in linewidth dominated, one would expect a correlation between  $R_{13}$  and galaxy inclination which is not seen (Sage & Isbell 1991; Paglione et al. 2001). It is unlikely, therefore, that broadened linewidths are the reason for the high  $R_{13}$ .

Alternatively,  $R_{13}$  can be increased by reducing the gas density. Due to radiative trapping, the critical density of CO is much lower than for  $^{13}\text{CO}$  or  $\text{C}^{18}\text{O}$ . The critical density for the  $^{13}\text{CO}$  line is  $n_{cr} \simeq 2 \times 10^3 \text{ cm}^{-3}$ , compared to  $2 \times 10^3 / \tau_{12\text{CO}} \text{ cm}^{-3}$ , or typically  $\sim 300 \text{ cm}^{-3}$ , for CO. Line intensities drop rapidly when the gas density is below the critical density. At densities of a few hundred  $\text{cm}^{-3}$  CO is still bright but  $^{13}\text{CO}$  and  $\text{C}^{18}\text{O}$  are subthermally excited and faint. Moreover, at such low densities intensities of the dense gas tracers such as HCN ( $n_{cr} \sim 10^{5-6} / \tau_{\text{HCN}} \text{ cm}^{-3}$ ) decrease dramatically. This scenario explains well the overall structure of  $R_{13}$  in NGC 6946 and in IC 342 (Meier, Turner & Hurt 2000; Meier & Turner 2001). In fact, in galaxies with gas densities of  $\sim 10^3 \text{ cm}^{-3}$ , the isotopomers become powerful density probes (note that the  $R_{13}$  contours are approximately horizontal in Figure 7 at densities below  $\sim 10^4 \text{ cm}^{-3}$ ). This also provides a natural explanation for the “underluminosity” of  $^{13}\text{CO}$  versus “overluminous” CO typically seen in distant starbursts (Taniguchi & Ohyama 1998).

#### 4.4.2. High $R_{13}$ from Abundance Variations

The second major class of models that produce enhanced  $R_{13}$  are caused by changing molecular abundances. The CO opacity can be lowered by decreasing the overall  $[\text{CO}/\text{H}_2]$  abundance. This is unlikely given the active star formation history and high metallicity of the nucleus ( $3 Z_{\odot}$ ; Belley & Roy 1992). Moreover, since CO is optically thick  $[\text{CO}/\text{H}_2]$  must be decreased by a large amount before a strong effect is seen in  $R_{13}$ . Decreasing the isotopic abundances equate directly to changes in  $R_i$  due to their low opacity, so changes in the relative isotopic abundances have a much more direct impact on  $R_i$ . Several methods of changing the isotopic abundances are considered in turn.

One way to raise the  $[\text{CO}/^{13}\text{CO}]$  abundance ratio is from the inflow of  $^{13}\text{CO}$ -poor molecular gas from the galactic disk. In the Galaxy, the  $[\text{CO}/^{13}\text{CO}]$  abundance ratio increases with galactocentric distance (eg. Wilson & Rood 1994; Wilson 1999). Driving  $^{13}\text{CO}$ -poor gas into the nucleus could raise the average  $[\text{CO}/^{13}\text{CO}]$ . NGC 6946 is a barred galaxy, and bars promote radial gas flow, which also tends to smooth out radial abundance variations (eg. Alloin et al. 1981; Friedli, Benz, & Kennicutt 1994). Flat abundance profiles over the central 2.5 kpc of NGC 6946 are already established for N and O (Belley & Roy 1992). Therefore, it is possible that the average  $[\text{CO}/^{13}\text{CO}]$  abundance ratio over the region is slightly high compared to Galactic ratios (as suggested by the LVG analysis). However, the abundance ratio should be well mixed over the whole nuclear region,

while in fact, in both NGC 6946 and IC 342, nuclear  $R_{13}$  values are significantly larger than those found in the disk (Paglione et al. 2001). So even if gas inflow is important it still requires that the molecular gas undergo a change in physical conditions as it enters the nuclear region in order to explain the increase in  $R_{13}$ . Additionally,  $[\text{CO}/\text{C}^{18}\text{O}]$  increases with Galactocentric distance with a slope steeper than  $[\text{CO}/^{13}\text{CO}]$ . Hence, if inflow alone was the determining factor, the  $^{13}\text{CO}/\text{C}^{18}\text{O}$  ratio would be expected to be driven to even higher values, more typical of galactic disks,  $\gtrsim 5$ . In fact, the opposite is seen.

Isotopic abundances can also be changed by chemical fractionation and/or isotope-selective photodissociation. Chemical fractionation imparts a chemical formation bias towards  $^{13}\text{CO}$  over CO when gas is cold and ion-molecule chemistry dominates (significantly below 35 K; eg. Langer et al. 1980, 1984), while isotope-selective photodissociation lowers the isotopomer abundances relative to the main isotopomer because of decreased self-shielding (eg. van Dishoeck & Black 1988). It is questionable whether chemical fractionation is relevant here since the molecular gas is mostly 35 K or warmer (§4.1). Moreover,  $R_{13}$  does not correlate with star formation (Figure 8a). The locations of the highest  $R_{13}$  are well away from the starburst site, where the gas is presumably cooler. Likewise for isotope-selective photodissociation. We dismiss both possibilities as controlling factors of the global  $R_{13}$  morphology. But we note that if the low  $R_{13}$  and  $R_{18}$  seen towards the eastern edge of the central ring are typical of physical conditions in the central ring in the absence of strong star formation then the slightly higher ratios, observed locally towards the starburst western edge of the ring, could result from localized selective photodissociation of  $^{13}\text{CO}$  and  $\text{C}^{18}\text{O}$ .

A final possibility for  $R_{13}$  enhancement due to variable molecular abundances is enrichment due to ejecta from massive stars. Though still somewhat uncertain, massive stars are predicted to pollute the nuclear ISM with  $^{12}\text{C}$  and potentially  $^{18}\text{O}$ , primarily early on in a starburst, with  $^{13}\text{C}$  following later as intermediate mass stars evolve off the main sequence (eg., Wilson & Matteucci 1992; Henkel & Mauersberger 1993; Prantzos, Aubert & Audouze 1996; Romano & Matteucci 2003). Enhancement of  $^{12}\text{C}$  and  $^{18}\text{O}$  at the expense of  $^{13}\text{C}$  in young systems is expected if the starburst IMF is biased to massive stars (as suggested for NGC 6946, Engelbracht et al. 1996). If the newly generated  $^{12}\text{C}$  and  $^{18}\text{O}$  is incorporated back into CO rapidly then CO and  $\text{C}^{18}\text{O}$  will be enhanced relative to  $^{13}\text{CO}$ , raising  $R_{13}$ , leaving  $R_{18}$  relatively unaffected, and lowering the  $^{13}\text{CO}/\text{C}^{18}\text{O}$  ratio. A combination of low opacity in the isotopomers and a relatively low  $^{13}\text{CO}/\text{C}^{18}\text{O}$  ratio implies that  $[\text{CO}/\text{C}^{18}\text{O}] \sim 2 - 3$  in the nucleus of NGC 6946. As discussed in §4.1, this provides some evidence that more applicable isotopic abundances are  $[\text{CO}/^{13}\text{CO}] \sim 60$  and  $[\text{CO}/\text{C}^{18}\text{O}] \sim 150$ , and  $[\text{CO}/\text{C}^{18}\text{O}] \sim 2.5$ . The  $[\text{CO}/\text{C}^{18}\text{O}]$  abundance ratio is significantly lower than the solar value of  $\sim 6$ , the Galactic center value of  $\sim 10$  and typical nearby galaxy nuclear values of 4. Thus it is possible that the somewhat low  $[\text{CO}/\text{C}^{18}\text{O}]$  value combined with the absence of a tight spatial correlation with the starburst indicates that the entire nuclear region is modestly enriched in CO and  $\text{C}^{18}\text{O}$  as compared to  $^{13}\text{CO}$ . Orbital timescales are 8 Myr for the central ring and 28 Myr at the edge of the field of view, much shorter than the lifetime of intermediate mass stars but comparable to the estimated starburst age of 7 - 20 Myr (Engelbracht et al. 1996). If

the ejecta can immediately return to the ambient ISM then interstellar enrichments probably has had time to spatially mix, providing an explanation for the globally low  $^{13}\text{CO}/\text{C}^{18}\text{O}$  line ratio. Abundances anomalies may, therefore, explain the globally low  $\text{CO}/\text{C}^{18}\text{O}$  and  $^{13}\text{CO}/\text{C}^{18}\text{O}$  ratios, but not their spatial variation.

In summary, from the close connection between  $R_{13}$  and HCN intensities combined with the overall inadequacies of all other explanations, it appears that the most likely explanation for the distribution of large  $R_{13}$  and  $R_{18}$  gas in the nucleus of NGC 6946 is a significant and coherent decrease in gas density as one moves away from the central ring, causing the isotopomers to become subthermal and faint relative to the main species, which remains thermal, opaque, and bright. Operating in tandem with higher temperatures or anomalous abundances that are peculiar to the nuclear environment, a small reduction in opacity at low gas densities can increase  $R_{13}$  substantially. The molecular arms in the inner 300 pc region appear to consist of a warm, low density gas that abruptly transitions to warmer, dense gas in the central ring. So the observed  $R_{13}$  is likely best considered a probe of the mixing fraction of dense, low  $R_{13}$  gas and diffuse, high  $R_{13}$  gas (Aalto et al. 1995; Sakamoto et al. 1997). HCN(1-0) emission probes the hotter, high density cores embedded inside the diffuse medium. Since there is no global correlation between  $R_{13}$  and HCN(3-2)/HCN(1-0) (Paglione et al. 2001), a tracer of the density of the dense gas component,  $R_{13}$  does not appear strongly sensitive to the exact density of the dense component.

#### 4.5. High $R_{13}$ : Bars as Redistributors of Gas Physical Conditions?

We find that the two gas components with distinctly different properties ( $n_{\text{H}_2}$  and  $T_K$ ) that are required to explain the single-dish line ratios in NGC 6946 are also found in distinctly different parts of the nucleus. Molecular gas with high  $R_{13}$  tends to be located along and upstream of the arms. The correlation of gas properties with position along a molecular bar was first noted by Wright et al. (1993), in IC 342. Similar features are now seen here in NGC 6946, Maffei 2 (Meier, Turner & Hurt 2004, in preparation), as well as the much larger-scale bars, UGC 2855 and NGC 7479 (Hüttemeister, Aalto, & Wall 1999; Hüttemeister et al. 2000). The morphology of  $R_{13}$  in barred galaxies such as NGC 6946 suggests that changes in  $R_{13}$  are connected to the dynamics but not through dynamical changes in linewidth. It must result instead from a mechanism capable of dispersing the molecular gas into spatially distinct regions of low density, diffuse emission and high density cloud cores, correlated with position across the bar. The theoretically predicted “spray regions” in barred potentials (Athanasoulas 1992) provide a natural explanation for the presence and locations of the extended, low density gas component inferred from the regions of high  $R_{13}$ . Dense gas is associated with the central  $x_2$ -type orbits and the cuspy ends of the  $x_1$ -type orbits, while the remaining molecular gas is “scattered” off the  $x_2$ -orbitals, putting the diffuse gas at and upstream of the molecular arms (as illustrated in Figure 9). In the case of IC 342, which has a higher column density (and density) in the arms,  $^{13}\text{CO}$  and  $\text{C}^{18}\text{O}$  extend further along the arms than in NGC 6946. In fact, in IC 342, the densities are such that one can trace the density



progression across the molecular arm from the upstream side up to the (shocked) leading edge (Wright et al. 1993; Meier & Turner 2001). Evidently, bars acting to disperse molecular gas into distinct regions with different physical conditions may be a common phenomena. This dynamical interpretation further supports the notion that the large  $R_{13}$  seen in distant mergers reflect changes in gas physical conditions associated with the large-scale dynamical redistribution of molecular gas. Though in this case, the redistribution would not be from a barred potential but from the action of the merger, directly.

#### 4.6. High $R_{13}$ : Comparisons to Distant Galaxies and ULIRGs

The resolved structure of NGC 6946 appears to be similar, but more modest version of the structure inferred for the ISM of ULIRGs (eg., Solomon et al. 1997; Downes & Solomon 1998). The diffuse arms in NGC 6946 appear to be cooler, lower column density analogues of the low density, high filling factor CO gas common in ULIRGs, while the starburst regions that are bright in HCN and  $^{13}\text{CO}$  in NGC 6946 are the more modest counterparts of the “extreme starbursts” seen in ULIRGs (Downes & Solomon 1998).

The ratio of CO to HCN luminosity is  $\sim 4\text{--}7$  in ULIRGs as compared to  $\sim 30\text{--}70$  in the disk of our Galaxy and normal galaxies (eg., Solomon, Downes & Radford 1992; Sorai et al. 2002). The low absolute CO/HCN ratio in ULIRGs argues strongly that the fraction of the mass in the dense component is much higher than in more modest starbursts like NGC 6946 (Solomon, Downes & Radford 1992). However, this exacerbates the problem of explaining the high observed  $R_{13}$ . Just requiring a large filling factor, diffuse component along with low filling factor embedded dense cores, like seen in NGC 6946, is not enough to simultaneously explain both the low CO/HCN and high  $R_{13}$  ratios in ULIRGs, for any reasonable  $[\text{CO}/^{13}\text{CO}]$  abundance. Evidently, one must also require that  $^{13}\text{CO}/\text{HCN}$  be significantly lower than the unity observed for NGC 6946’s dense component. This can be achieved by a large opacity in the HCN(1-0) transition.

The relative opacity of lines with similar frequencies and upper energy levels (as is the case for the J=1-0 transitions of CO,  $^{13}\text{CO}$ ,  $\text{C}^{18}\text{O}$  and HCN) depend primarily on their relative abundances and transition line strengths (proportional to the dipole moment squared,  $|\mu|^2$ ). In gas with densities high enough to thermalize HCN (and consequently CO and  $^{13}\text{CO}$ ), (eg. Kohno, Kawabe, & Vila-Vilaró 1999):

$$\frac{\tau_{\text{HCN}}}{\tau_{^{13}\text{CO}}} \simeq \left[ \frac{\text{HCN}}{^{13}\text{CO}} \right] \left( \frac{\mu_{\text{HCN}}}{\mu_{^{13}\text{CO}}} \right)^2 \sim 10, \quad (3)$$

given expected HCN abundances. Hence, the opacity of HCN can significantly exceed the opacity of  $^{13}\text{CO}$  in warm, dense regions (eg., Aalto et al. 1997). For example, based on our LVG models (§4.1), for  $T_k = 150$  K,  $n_{H_2} = 10^5$ ,  $[^{13}\text{CO}/\Delta v] = 10^{-6.4}$  and  $[\text{HCN}/\Delta v] = 10^{-8.3}$ ,  $^{13}\text{CO}(1\text{--}0)/\text{HCN}(1\text{--}0) \simeq 0.3$ . This value can be decreased even more if one lowers the  $[\text{CO}/^{13}\text{CO}]$  abundance below that adopted for NGC 6946 (stronger isotope-selective photodissociation?). For the localized dense cores, CO and HCN can be bright due to high opacity, while the optically thin  $^{13}\text{CO}$  remains relatively

faint. Assuming these dense cores are embedded in a low density medium with a much larger filling factor, then it becomes possible to simultaneously explain low beam averaged CO/HCN and CO(2-1)/CO(1-0) line ratios while maintaining high beam-averaged  $R_{13}$  ratios. Given the fairly high excitation required, it makes sense that this would be seen primarily in the “extreme starburst” cores associated with ULIRGs.

## 5. Conclusions

Aperture synthesis maps of  $^{13}\text{CO}$  and  $\text{C}^{18}\text{O}$  in the nucleus of NGC 6946 are presented. The gas morphology and kinematics are consistent with molecular gas moving in response to a barred potential. The emission from  $^{13}\text{CO}$  and  $\text{C}^{18}\text{O}$  is more symmetric and confined to the central ring of molecular material than is CO. Because of this,  $R_{13}$  (ratio of integrated intensity,  $^{12}\text{CO}/^{13}\text{CO}$ ,  $J=1-0$  for both) and  $R_{18}$  ( $^{12}\text{CO}/^{18}\text{CO}$ ,  $J=1-0$ ) increase dramatically moving away from the central starburst, particularly along and to the trailing side of the CO bright northern molecular arm.  $R_{13}$  reaches measured values as high as 30, more than three times higher than Galactic values, and upper limits significantly higher yet in some parts of this region. The transition between low  $R_{13}$  gas and high  $R_{13}$  gas is very sharp once the central ring is left, indicating a very rapid change in physical conditions.

If  $^{13}\text{CO}$  and  $\text{C}^{18}\text{O}$  accurately trace the amount of molecular gas present, the standard conversion factor,  $X_{\text{CO}}$ , in NGC 6946 must be lower than the Galactic value. Column densities inferred from  $^{13}\text{CO}$ ,  $\text{C}^{18}\text{O}$ , and 1.4 mm dust continuum emission imply that  $X_{\text{CO}}(6946)$  is  $\sim 1/3 - 1/5$  the Galactic value at the sites of the GMCs, for a typical value of  $X_{\text{CO}} = 0.5 \times 10^{20} \text{ cm}^{-2} (\text{K km s}^{-1})^{-1}$ . Towards the diffuse gas component along the northern arm, the conversion factor is likely a factor of 2 - 3 lower yet. Star formation as traced by 2.7 mm continuum and  $\text{P}\alpha$  more closely follows total gas surface density (or perhaps density) traced by the isotopomers rather than the optically thick CO intensity. The total gas mass in the central 175 kpc radius of NGC 6946 is  $\sim 1 \times 10^8 M_{\odot}$ , and the star formation efficiency on 100 pc sizescales is a few percent.

Both gas moving with large radial velocities ( $v_r \simeq 80 \text{ km s}^{-1}$ ) and bright HCN(1-0) emission imply that molecular gas has piled up along the central ring. LVG models find best fit densities of  $n_{\text{H}_2} \sim 10^{4.2} \text{ cm}^{-3}$  towards the central molecular ring and densities below  $n_{\text{H}_2} \lesssim 10^2 \text{ cm}^{-3}$  along the northern arm. Corresponding kinetic temperatures are  $T_k \sim 90 \text{ K}$  for the central starburst and  $T_k \lesssim 40 \text{ K}$  for northern arm. The morphology of the isotopomers are very similar to the high critical density tracer HCN(1-0), demonstrating that density changes are a key physical condition governing the local changes in  $R_{13}$ . Together with the fact that  $R_{13}$  is correlated with position relative to the bar, this suggests that the bar potential acts to disperse the molecular gas into coherent regions with different physical conditions. Here in NGC 6946, the high  $R_{13}$  line ratio values are a signpost of a dynamically evolving ISM. Applying these findings regarding the ISM structure of NGC 6946 to other more distant starbursts can successfully explain some of their observed molecular properties, hinting that similar processes may be at work there too.

We are grateful to the faculty and staff at OVRO for their support and assistance during the observations. We thank Eva Schinnerer for helpful discussions and S. Ishizuki for the use of his  $^{12}\text{CO}(1-0)$  data on NGC 6946. We also thank an anonymous referee for providing a critical reading of the manuscript. This work is supported in part by NSF grant AST-0071276 to JLT. DSM acknowledges support from NSF grant 1-5-29627 to the Laboratory of Astronomical Imaging at the University of Illinois. The Owens Valley Millimeter Interferometer is operated by Caltech with support from the NSF under Grant 9981546.

## REFERENCES

- Aalto, S., Booth, R. S., Black, J. H. & Johansson, L. E. B. 1995, *A&A*, 300, 369
- Aalto, S., Booth, R. S., Johansson, L. E. B., & Black, J. H. 1991, *A&A*, 247, 291
- Aalto, S., Radford, S. J. E., Scoville, N. Z., & Sargent, A. I. 1997, *ApJ*, 475, L107
- Alloin, D., Edmunds, M. G., Lindblad, P. O., & Pagel, B. E. J. 1981, *A&A*, 101, 377
- Arp, H. 1966, *ApJS*, 14, 1
- Athanassoula, E. 1992, *MNRAS*, 259, 328
- Ball, R., Sargent, A. I., Scoville, N. Z., Lo, K. Y. & Scott, S. L. 1985, *ApJ*, 298, L21
- Belley, J. & Roy, J. 1992, *ApJS*, 78, 61
- Binney, J. & Tremaine, S. 1987, Princeton, NJ, Princeton University Press, 1987, p.,
- Böker, T. et al. 1999, *ApJS*, 124, 95
- Bohlin, R. C., Savage, B. D. & Drake, J. F. 1978, *ApJ*, 224, 132
- Carlstrom, J. E., Jackson, J. M., Turner, J. L. & Ho, P. T. P. 1990, in *The Interstellar Medium in External Galaxies*, ed. D. J. Hollenbach & H. A. Thronson (NASA Conf. Publ. 3084, 337
- Casoli, F., Dupraz, C., & Combes, F. 1992, *A&A*, 264, 55
- Dahmen, G., Hüttemeister, S., Wilson, T. L., & Mauersberger, R. 1998, *A&A*, 264, 55
- de Jong, T., Dalgarno, A., & Chu, S.-I. 1975, *ApJ*, 199, 69
- de Vaucouleurs, G., de Vaucouleurs, A., & Corwin, H. G 1976, *Second Reference Catalog of Bright Galaxies* (Austin:Unvi. Texas Press) (RC2)
- Downes, D. & Solomon, P. M. 1998, *ApJ*, 507, 615
- Elmegreen, D. M., Chromey, F. R. & Santos, M. 1998, *AJ*, 116, 1221

- Engargiola, G. 1991, ApJS, 76, 875
- Engelbracht, C. W., Rieke, M. J., Rieke, G. H., & Latter, W. B. 1996, ApJ, 467, 227
- Friedli, D., Benz, W., & Kennicutt, R. 1994, ApJ, 430, L105
- Frerking, M. A., Langer, W. D. & Wilson, R. W. 1982, ApJ, 262, 59
- Gao, Y., & Solomon, P. 2003, to appear in *Star Formation at High Resolution*, ed. R. Jayawardhana, M. G. Burton, & T. L. Bourke (San Francisco: ASP Conf. Series)
- Glenn, J. & Hunter, T. R. 2001, ApJS, 135, 177
- Goldreich, P. & Kwan, J. 1974, ApJ, 189, 441
- Goldsmith, P. F., Bergin, E. A., & Lis, D. C. 1997, ApJ, 491, 615
- Green, S. & Thaddeus, P. 1974, ApJ, 191, 653
- Helfer, T. T. & Blitz, L. 1997, ApJ, 478, 233
- Helfer, T. T., Thornley, M. D., Regan, M. W., Wong, T., Sheth, K., Vogel, S. N., Blitz, L., & Bock, D. C.-J. 2003, ApJS, 145, 259
- Henkel, C. & Mauersberger, R. 1993, A&A, 274, 730
- Hildebrand, R. H. 1983, QJRAS, 24, 267
- Ho, P. T. P., Turner, J. L., & Martin, R. N. 1987, ApJ, 322, L67
- Hüttemeister, S., Aalto, S., Das, M., & Wall, W. F. 2000, A&A, 363, 93
- Hüttemeister, S., Aalto, S., & Wall, W. F. 1999, A&A, 346, 45
- Hunter, S. D. et al. 1997, ApJ, 481, 205
- Irvine, W. M., Goldsmith, P. F., & Hjalmarsen, A. 1987, ASSL Vol.134: Interstellar Processes, 561
- Ishizuki, S., Kawabe, R., Ishiguro, M., Okumura, S. K., Morita, K.-I., Chikada, Y., Kasuga, T., & Doi, M. 1990b, ApJ, 355, 436
- Israel, F. P. & Baas, F. 2001, A&A, 371, 433
- Kennicutt, R. C. 1989, ApJ, 344, 685
- Kim, K.-T. & Koo, B.-C. 2003, ApJ, 595, 362
- Kohno, K., Kawabe, R., & Vila-Vilaró, B. 1999, ApJ, 511, 157
- Langer, W. D., Goldsmith, P. F., Carlson, E. R., & Wilson, R. W. 1980, ApJ, 235, L39

- Langer, W. D., Graedel, T. E., Frerking, M. A., & Armentrout, P. B. 1984, *ApJ*, 277, 581
- Leisawitz, D., Bash, F. N., & Thaddeus, P. 1989, *ApJS*, 70, 731
- MacLaren, I., Richardson, K. M., & Wolfendale, A. W. 1988, *ApJ*, 333, 821
- Meier, D. S. & Turner, J. L. 2001, *ApJ*, 551, 687
- Meier, D. S., Turner, J. L. & Hurt, R. L. 2000, *ApJ*, 531, 200
- Mezger, P. G. & Henderson, A. P. 1967, *ApJ*, 147, 471
- Myers, P. C., Dame, T. M., Thaddeus, P., Cohen, R. S., Silverberg, R. F., Dwek, E., & Hauser, M. G. 1986, *ApJ*, 301, 398
- Neininger, N., Guelin, M., Klein, U., Garcia-Burillo, S., & Wielebinski, R. 1998, *A&A*, 339, 737
- Nguyen-Q.-Rieu, Jackson, J. M., Henkel, C., Truong, B., & Mauersberger, R. 1992, *ApJ*, 399, 521
- Nguyen-Q.-Rieu, Nakai, N., & Jackson, J. M. 1989, *A&A*, 220, 57
- Nieten, C., Dumke, M., Beck, R. & Wielebinski, R. 1999, *A&A*, 347, L5
- Okumura, S. K., Kawabe, R., Ishiguro, M., Kasuga, T., Morita, K.-L. & Ishizuki, S. 1991, *IAU* 146 425
- Padin, S., Scott, S. L., Woody, D. P., Scoville, N. Z., Seling, T. V., Finch, R. P., Ciovanine, C. J., & Lowrance, R. P. 1991, *PASP*, 103, 461
- Paglione, T. A. D. et al. 2001, *ApJS*, 135, 183
- Paglione, T. A. D., Jackson, J. M., Bolatto, A. D., & Heyer, M. H. 1998, *ApJ*, 493, 680
- Papadopoulos, P. P. & Ivison, R. J. 2002, *ApJ*, 564, L9
- Polk, K. S., Knapp, G. R., Stark, A. A., & Wilson, R. W. 1988, *ApJ*, 332, 432
- Pollack, J. B., Hollenbach, D., Beckwith, S., Simonelli, D. P., Roush, T. & Fong, W. 1994, *ApJ*, 421, 615
- Prantzos, N., Aubert, O., & Audouze, J. 1996, *A&A*, 309, 760
- Radford, S. J. E., Downes, D. & Solomon, P. M. 1991, *ApJ*, 368, L15
- Regan, M. W. 2000, *ApJ*, 541, 142
- Regan, M. W. & Vogel, S. N. 1995, *ApJ*, 452, L21
- Rieke, G. H. & Lebofsky, M. J. 1978, *ApJ*, 220, L37

- Romano, D. & Matteucci, F. 2003, MNRAS, 342, 185
- Sage, L. J. & Isbell, D. W. 1991, A&A, 247, 320
- Sakamoto, S., Handa, T., Sofue, Y., Honma, M., & Sorai, K. 1997, ApJ, 475, 134
- Sakamoto, K., Okumura, S. K., Ishizuki, S. & Scoville, N. Z. 1999, ApJS, 124, 403
- Scoville, N. Z., Carlstrom, J., Padin, S., Sargent, A., Scott, S. & Woody, D. 1994, Astronomy with Millimeter and Submillimeter Wave Interferometry, IAU Colloquium 140, ASP Conference Series, Vol. 59, 1994, M. Ishiguro and J. Welch, Eds., p.10
- Scoville, N. Z., Sargent, A. I., Sanders, D. B. & Soifer, B. T. 1991, ApJ, 365, L5
- Scoville, N. Z. & Solomon, P. M. 1974, ApJ, 187, L67
- Sofue, Y., Doi, M., Ishizuki, S., Nakai, N., & Handa, T. 1988, PASJ, 40, 511
- Solomon, P. M., Downes, D. & Radford, S. J. E. 1992, ApJ, 387, L55
- Solomon, P. M., Downes, D., Radford, S. J. E., & Barrett, J. W. 1997, ApJ, 478, 144
- Sorai, K., Nakai, N., Kuno, N., & Nishiyama, K. 2002, PASJ, 54, 179
- Strong et al. 1988, A&A, 207,1
- Taniguchi, Y. & Ohyama Y. 1998, ApJ, 507, L121
- Taniguchi, Y., Ohyama Y. & Sanders D. B. 1999, ApJ, 522, 214
- Tully, R. B. & Fisher, J. R. 1988, Catalog of Nearby Galaxies, Cambridge Univ. Press, 1988
- Turner, J. L. & Ho, P. T. P. 1983, ApJ, 268, L79
- Turner, J. L. & Hurt, R. L. 1992, ApJ, 384, 72
- Turner, J. L., Martin, R. N., & Ho, P. T. P. 1990, ApJ, 351, 418
- Vacca, W. D., Garmany, C. C. & Shull, J. M. 1996, ApJ, 460, 914
- van Dishoeck, E. F., & Black, J. H. 1988, ApJ, 334, 771
- Wall, W. F., Jaffe, D. T., Bash, F. N., Israel, F. P., Maloney, P.R., & Baas, F. 1993, ApJ, 414, 98
- Walsh, W., Beck, R., Thuma, G., Weiß, A., Wielebinski, R., & Dumke, M. 2002, A&A, 388, 7
- Weiß, A., Neininger, N., Hüttemeister, S., & Klein, U. 2001, A&A, 365, 571
- Weliachew, L., Casoli, F. & Combes, F. 1988, A&A, 199, 29

- Wilson, C. D. & Scoville, N. Z. 1990, *ApJ*, 363, 435
- Wilson, T. L. 1999, *Rep. Prog. Phys.*, 62, 143
- Wilson, T. L. & Matteucci, F. 1992, *A&A Rev.*, 4, 1
- Wilson, T. L. & Rood, R. 1994, *ARA&A*, 32, 191
- Wright, M. C. H., Ishizuki, S., Turner, J. L., Ho, P. T. P., & Lo, K. Y. 1993, *ApJ*, 406, 470

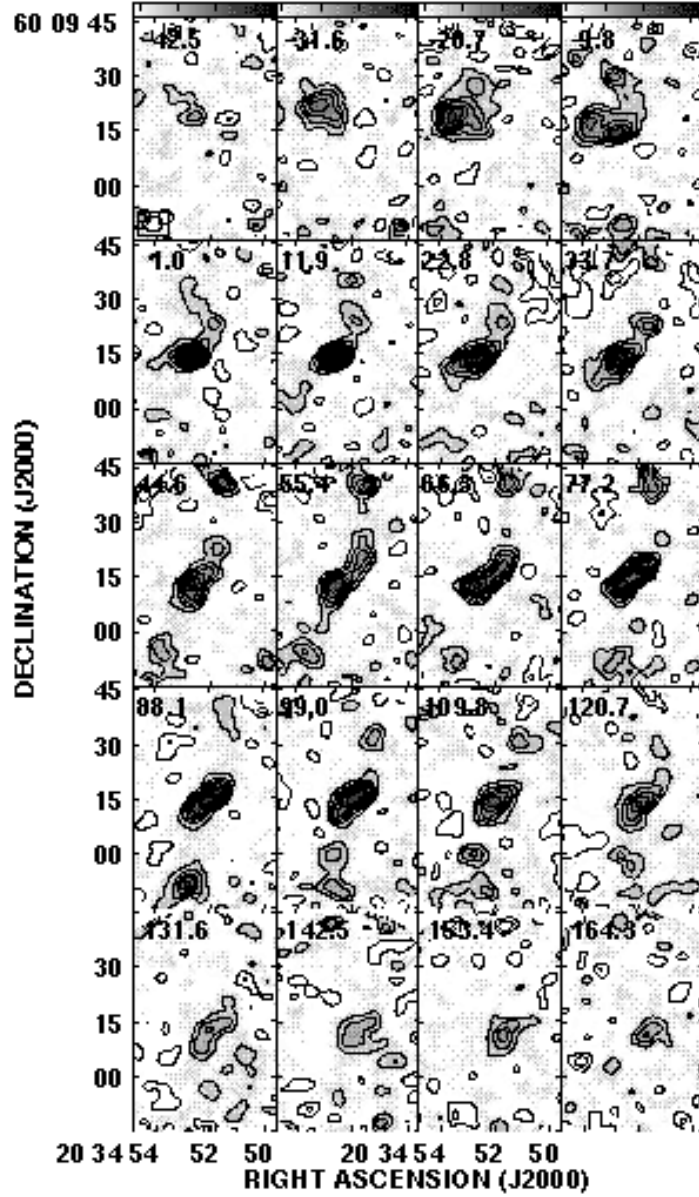


Fig. 1.—  $^{13}\text{CO}(1-0)$  channel maps for the nucleus of NGC 6946. LSR velocities are listed at the top of each panel. The contours are plotted in intervals of  $20 \text{ mJy } \text{bm}^{-1}$  (or  $0.09 \text{ K}$  for the  $5.''4 \times 4.''2$  beam) corresponding to  $2\sigma$ . The beam is plotted in the bottom left of the first panel.



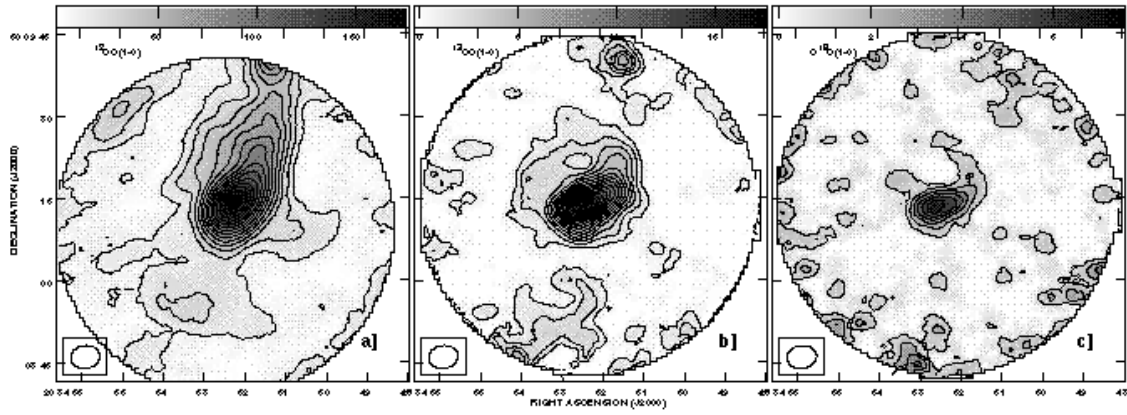


Fig. 2.— The CO isotopomers integrated intensity maps of NGC 6946. (a) The  $^{12}\text{CO}(1-0)$  integrated intensity image from (Sakamoto et al. 1999) convolved to the resolution of the  $^{13}\text{CO}(1-0)$  transition ( $5.''4 \times 4.''2$ ). Contours are in steps of 50.0 K km s $^{-1}$ . (b) The  $^{13}\text{CO}(1-0)$  integrated intensity image. Contours are in steps of the  $2\sigma$  value of 4.5 K km s $^{-1}$ . (c) The  $\text{C}^{18}\text{O}(1-0)$  integrated intensity image. Contours are in steps of the  $2\sigma$  value of 4.5 K km s $^{-1}$  (with the same beamsize as in (a) - (b)).

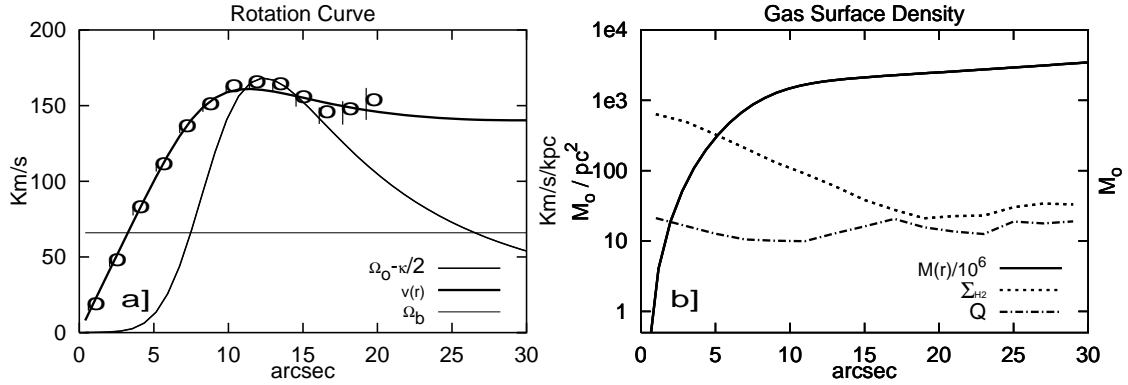


Fig. 3.— (a) The observed and fitted rotation curve of the central arcminute of NGC 6946. Circles mark the measured azimuthally averaged velocity versus radius, and short vertical bars are the uncertainty. The fitted model (thick solid line) consists of two mass distributions corresponding to Brandt rotation curves (see text for details). The pattern speed appropriate for the nucleus,  $\Omega_p = 66 \text{ km s}^{-1} \text{ kpc}^{-1}$  (thin solid line) is taken from (Crosthwaite & Turner 2004, in preparation), based on the large-scale disk velocity field traced by CO(1-0) and HI.  $\Omega_o$  is the angular velocity of the gas and  $\kappa$  is the epicyclic frequency. The intersections of  $\Omega_p$  with the  $\Omega_o - \kappa/2$  curve (dotted line) mark the locations of the iILR ( $\sim 7.5''$ ) and oILR ( $\sim 26''$ ) for this same pattern speed. (b) The observed azimuthally averaged molecular gas surface density,  $\Sigma_{H_2}$  (dotted line), based on the  $^{13}\text{CO}$  column density derived in §4.2 for the central  $30''$  is shown. The cumulative dynamical mass interior to a given radius based on the model rotation displayed in (a) is also shown (solid line). Given the rotation curve in (a) and the gas surface density, we calculate and display the Toomre  $Q$  parameter (dot-dashed line) for the central region of NGC 6946. The surface density axis is on the lefthand side, while the dynamical mass axis is on the righthand side in units of  $10^6 M_\odot$ .  $Q$  uses the same axis as surface density but is unitless. All rotation curve data has been corrected for inclination.

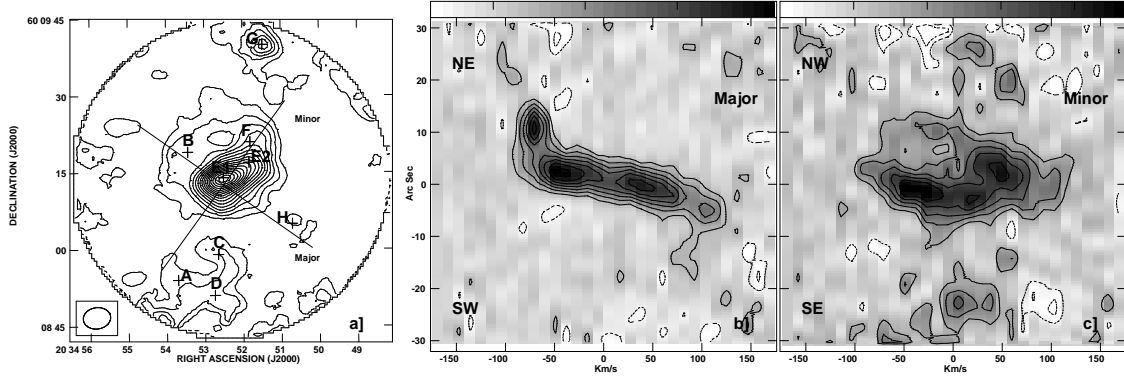


Fig. 4.— The Position-Velocity (PV) diagrams of NGC 6946 taken from the  $^{13}\text{CO}(1-0)$  data. (a) The  $^{13}\text{CO}(1-0)$  integrated intensity map of NGC 6946 contoured as in Figure 2b. Fitted GMCs are labeled on the figure as well as the locations the PV slices have been measured at. The PV diagram for the (b) major, (c) minor axes. PV diagrams are contoured in steps of  $3\sigma$

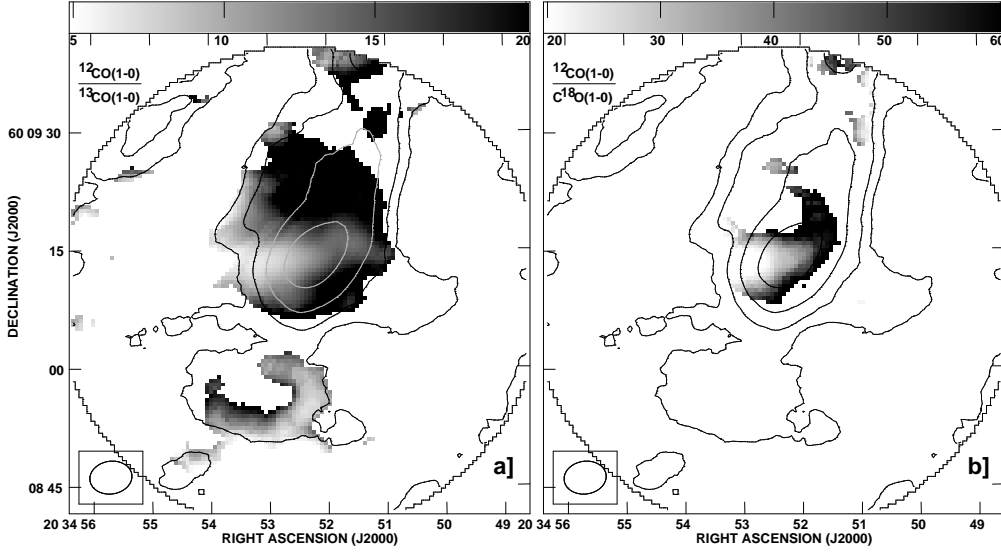


Fig. 5.— The isotopic line ratios in NGC 6946. (a) The  $^{12}\text{CO}(1-0)/^{13}\text{CO}(1-0)$  line ratio ( $R_{13}$ ). The  $^{12}\text{CO}(1-0)$  data has been kindly provided by Sakamoto et al. (1999). High ratios are dark. The greyscale ranges from 5 - 20. Contours are  $^{12}\text{CO}(1-0)$  in steps of  $75 \text{ K km s}^{-1}$ . The ratio map has been blanked in regions where either map is less than  $3\sigma$  in intensity. In almost all cases, the transition that limits the field is the weaker  $^{13}\text{CO}(1-0)$ , therefore any region inside the  $^{12}\text{CO}(1-0)$  contours that is blanked also has very high line ratios. (c) The  $^{12}\text{CO}(1-0)/\text{C}^{18}\text{O}(1-0)$  line ratio ( $R_{18}$ ). Contouring and greyscaling are the same as (b) except that the greyscale ranges from 20 - 60. Again, the  $\text{C}^{18}\text{O}(1-0)$  transition is the cause of most the blanking, so blanked regions represent high ratio regions.

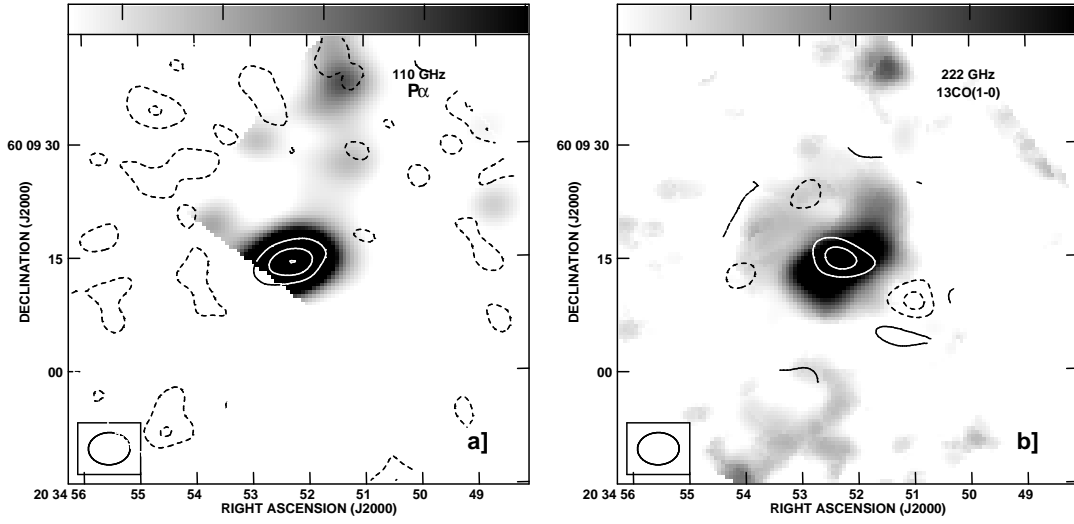


Fig. 6.— Millimeter continuum maps of the nucleus of NGC 6946. (a) The 110 GHz (2.7 mm) continuum map for NGC 6946 overlaid on the HST P $\alpha$  NICMOS image (Böker et al. 1999), smoothed to the same resolution. Contours are in steps of the  $2\sigma$  value of  $2.0 \text{ mJy bm}^{-1}$ . This map has been corrected for  $^{13}\text{CO}(1-0)$  contamination. (b) The 222 GHz (1.4 mm) continuum emission from NGC 6946 overlaid on the  $^{13}\text{CO}(1-0)$  greyscale. Contours are in steps of the  $2\sigma$  value of  $7 \text{ mJy bm}^{-1}$ .

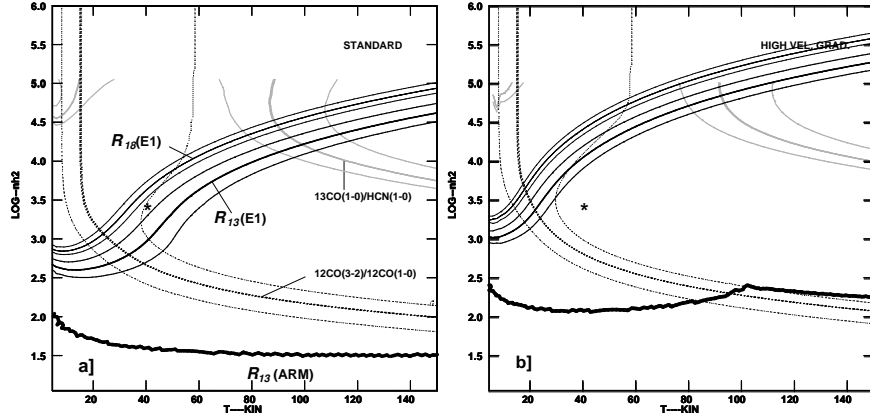


Fig. 7.— CO LVG Models. (a) LVG models for the  $R_{13}$  and  $R_{18}$  line ratios for a “standard” abundance per velocity gradient determined by  $^{12}\text{CO}/\text{H}_2 = 8.5 \times 10^{-4}$ , and  $dv/dr = 3.0 \text{ km s}^{-1} \text{ pc}^{-1}$  and  $[^{12}\text{CO}/^{13}\text{CO}] = 40$  and  $[^{12}\text{CO}/^{13}\text{CO}] = 150$ . The observed values towards E1 plus their  $\pm 1\sigma$  range of  $R_{13}$  and  $R_{18}$  are plotted (Table 5). The fact that the acceptable parameter space implied from  $R_{13}$  is slightly lower than that implied by  $R_{18}$ , suggests that  $[^{13}\text{CO}/\text{C}^{18}\text{O}]$  has been slightly overestimated. The two curves coincide for an abundance ratio of  $[\text{CO}/^{13}\text{CO}] \simeq 60$  and  $[\text{CO}/\text{C}^{18}\text{O}] \simeq 150$ . Also overlaid for reference is the location where the  $^{13}\text{CO}(1-0)/\text{HCN}(1-0)$  line ratio is unity assuming  $X_{\text{HCN}}/dv/dr = 1.5 \times 10^{-8}/3 \text{ km s}^{-1}$  (see text). The single-dish  $^{12}\text{CO}(3-2)/^{12}\text{CO}(1-0)$  line ratio is shown, along with an asterisk marking the derived kinetic temperature and density of (Walsh et al. 2002). Overlap of the large-scale  $\text{CO}(3-2)/\text{CO}(1-0)$  ratio with  $R_{13}(E1)$  gives an estimate of the large-scale average excitation. On the other hand, the overlap between  $R_{13}(E1)$  and  $^{13}\text{CO}(1-0)/\text{HCN}(1-0)$  gives an indication of the local ( $\sim 5''$ ) physical conditions toward E1. The  $R_{13} = 30$  contour is also displayed to show the constraint on the parameter space suitable for the molecular arm regions (labeled  $R_{13}(\text{ARM})$ ). Since along the arms,  $R_{13} \gtrsim 30$ , acceptable densities are  $n_{\text{H}_2} \lesssim 10^{1.8}$ . (b) Same plot as in (a) except for a velocity gradient (abundance) four times larger (smaller). This gives an indication of the sensitivity of the models to changes in abundance per velocity gradient, and may represent models more suitable to the large linewidth central molecular ring.

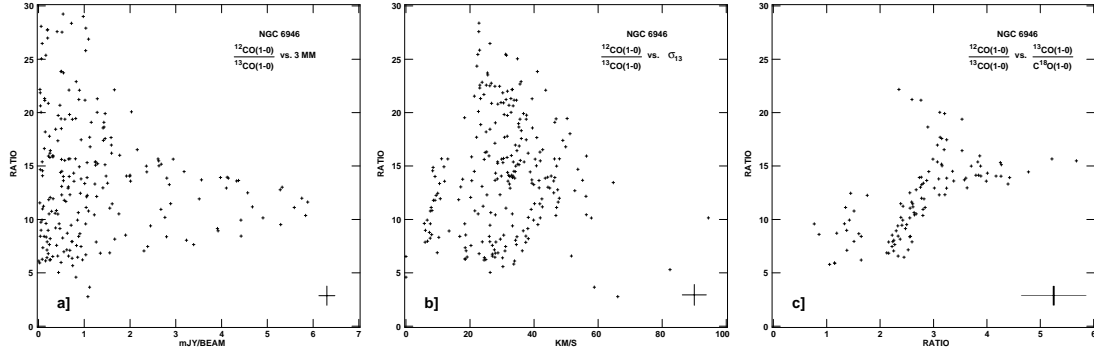


Fig. 8.— (a)  $R_{13}$  vs. 3 mm continuum sampled at  $1''$  intervals. The cross at the lower righthand corner of the figure displays representative errorbars for each point. (b) Same as (a) except for  $R_{13}$  vs.  $^{13}\text{CO}(1-0)$  velocity dispersion. (c) Same as (a) except for  $R_{13}$  vs.  $^{13}\text{CO}(1-0)/\text{C}^{18}\text{O}(1-0)$ . Note: Since the sampling rate is finer than the beamsize not all individual points are independent. Data is only displayed for the high S/N regions not blanked in Figure 5.

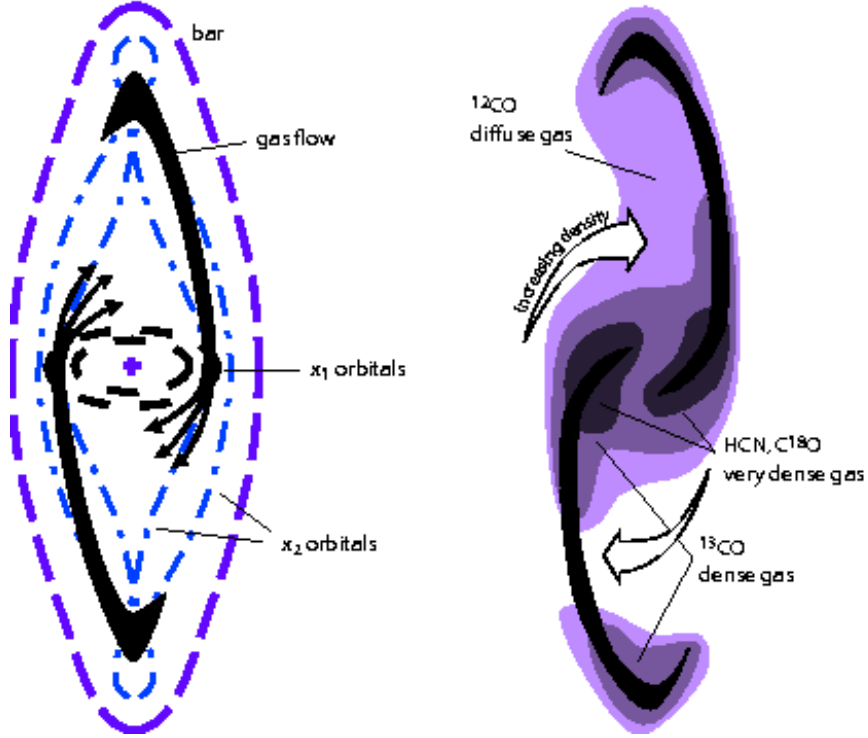


Fig. 9.— *Left*) The basic flow patterns of molecular gas in a barred potential (eg., Athanassoula 1992). *Right*) A schematic showing the distribution of components with different physical conditions in response to that barred potential. The densest gas, bright primarily in HCN and  $\text{C}^{18}\text{O}$  emission is confined to the intersection regions of the  $x_1$  and  $x_2$  regions, explaining the sort of “saddle” region seen in  $R_{13}$  and CO/HCN (Helfer & Blitz 1997).  $^{13}\text{CO}$  is seen primarily towards the central ring-like region as well as at the cuspy ends of the bar. CO, on the other hand, is remains bright over much of the entire region, tracing the distribution of the low density gas. The locations of the extended, low density gas component inferred from the regions of high  $R_{13}$  correspond to the theoretically predicted “spray regions” in barred potentials.



Table 1. NGC 6946 Basic Data

Characteristic	NGC 6946	Reference
Hubble Class	SAB(rs)cd	1
Near-IR Center:		
$\alpha(J2000)$	$20^h34^m52^s.34 \pm 0.2''$	2
$\delta(J2000)$	$+60^\circ09'13.''7 \pm 0.2''$	
Radio Continuum Peak:		
$\alpha(J2000)$	$20^h34^m52^s.20 \pm 0.2''$	3
$\delta(J2000)$	$+60^\circ09'14.''2 \pm 0.2''$	
Dynamical Center:		
$\alpha(J2000)$	$20^h34^m52^s.29 \pm 2''$	4
$\delta(J2000)$	$+60^\circ09'14.''5 \pm 2''$	
$V_{lsr}$	$50 \text{ km s}^{-1}$	4
Adopted Distance	5.2 Mpc	5
$i$	$40^\circ$	6
P.A.	$242^\circ$	6
$L_{IR}$	$1.5 \times 10^9 L_\odot$	7
$T_d$	40 K	7

References. — (1) RC2 (2) measured from 2MASS images (3) Turner & Ho 1983, Tsai et al. 2004, in preparation, 2 cm peak; (4) This paper; (5) Tully 1988; (6) Crosthwaite & Turner 2004, in preparation; (7) Engargiola 1991

Table 2. Observational Data<sup>a</sup>

Transition	$\nu_o$ (GHz)	$T_{sys}$ (K)	$\Delta V_{chan}$ (km s <sup>-1</sup> )	$\Delta \nu_{band}$ (MHz)	Beam ('';deg)	Noise level (mK/mJy Bm <sup>-1</sup> )
<sup>13</sup> CO(1-0)	110.20	240-380	10.88	128	5.4x4.2;-82	44/10
C <sup>18</sup> O(1-0)	109.78	240-380	10.92	128	5.5x4.4;-83	44/10
2.7 mm <sup>b</sup>	110.0	240-380	...	1000	5.5x4.3;-89	3.8/0.9
1.4 mm <sup>c</sup>	221.9	700-1600	...	1000	5.5x4.3;-89	3.7/5.5

<sup>a</sup>Dates for observations of NGC 6946 were 1999 September 26 - 1999 November 28, with a phase center:  $V_{LSR}=50 \text{ km s}^{-1}$   $\alpha = 20^h 33^m 49^s.20$ ,  $\delta = +59^\circ 58' 49.''0$  (B1950).

<sup>b</sup><sup>13</sup>CO(1-0) line contamination has been removed.

<sup>c</sup>Convolved to the resolution of 2.7 mm.

Table 3. Measured Intensities & Temperatures in NGC 6946<sup>a</sup>

GMC <sup>b</sup>	I( <sup>12</sup> CO(1-0)) <sup>c</sup> ( <i>K km s</i> <sup>-1</sup> )	I( <sup>13</sup> CO(1-0)) ( <i>K km s</i> <sup>-1</sup> )	T( <sup>13</sup> CO(1-0)) ( <i>K</i> )	I(C <sup>18</sup> O(1-0)) ( <i>K km s</i> <sup>-1</sup> )	T(C <sup>18</sup> O(1-0)) ( <i>K</i> )
A	100±16	6.4±2	0.28±0.05	<3.6	0.13±0.05
B	120±16	17±2	0.59±0.06	9.0±1.8	0.17±0.05
C	87±16	6.4±2	0.29±0.05	7.2±1.8	0.15±0.05
D	74±16	8.6±2	0.50±0.05	11±1.8	0.20±0.05
E1	650±65	64±6	0.82±0.08	31±3	0.33±0.05
E2	590±59	50±5	0.59±0.06	10±1.8	0.22±0.05
F	300±30	20±2	0.32±0.05	9.4±1.8	~0.11
G	300±30	20±2	0.45±0.05	<3.6	0.22±0.05
H	74±16	3.6±2	0.19±0.05	<3.6	<0.11
ARM <sup>d</sup>	270±27	4.7±2	0.14±0.05	<3.6	<0.11

<sup>a</sup>Uncertainties are the larger of the map uncertainty or the absolute calibration uncertainties. Upper limits are  $2\sigma$ .

<sup>b</sup>Positions are those labeled in Table 4 and Figure 4a.

<sup>c</sup>Taken from the Sakamoto et al. 1999 data.

<sup>d</sup>The position of the 'ARM' measurement corresponds to  $\alpha(J2000) = 20^h34^m51^s.20$ ,  $\delta(J2000) = +60^\circ09'28.''4$ .

Table 4. Giant Molecular Clouds in NGC 6946<sup>a</sup>

GMC	$\alpha, \delta$ ( $20^h34^m; 60^{\circ}09'$ )	$a \times b; pa$ ( $pc \times pc; ^{\circ}$ )	$\Delta v_{1/2}$ ( $km\ s^{-1}$ )	$v_o$ ( $km\ s^{-1}$ )	$M_{vir}^b$ ( $10^6\ M_{\odot}$ )	$^{13}M_{CO}^c$ ( $10^6\ M_{\odot}$ )
A	53.56;53.1 <sup>d</sup>	230x68;44	41	55	28	1.3
B	53.44;19.0	260x150;149	26	-19	18	8.6
C	52.68;59.6 <sup>d</sup>	110x<53 <sup>e</sup>	40	104	<16	1.2
D	52.85;51.4 <sup>d</sup>	290x140;90	35	91	33	4.4
E1	52.62;13.8	170x100;137	110	48	210	14
E2	51.93;15.9	270x<53;148 <sup>e</sup>	100	83	<160	9.2
F	51.74;22.9	110x68;28	97	37	110	3.9
G	51.52;40.0	180x140;68	46	62	44	6.6
H	50.72;05.9	150x66;35	22	133	6.4	0.66

<sup>a</sup>Typical fit uncertainties are less 1/2 the channel width of  $10.9\ K\ km\ s^{-1}$ , so an uncertainty of  $5.5\ K\ km\ s^{-1}$  is conservatively estimated.

<sup>b</sup>Based on  $189(\Delta v_{1/2; km/s})^2 R_{pc}$ , with R defined as  $1.4R_{FWHM}$ , or  $0.7\sqrt{ab}$  (eg. Meier & Turner 2001).

<sup>c</sup>Based on the molecular column density from  $^{13}CO(1-0)$  corrected for resolved out emission and He content, and the larger of the beamsize or fitted cloud size.

<sup>d</sup>Based on  $20^h34^m; 60^{\circ}08'$ .

<sup>e</sup>A GMC is considered unresolved if its deconvolved size is less than 1/2 of the beam minor axis.

Table 5. Observed Line Ratios in NGC 6946

GMC	$\frac{^{12}CO(1-0)}{^{13}CO(1-0)}$	$\frac{^{12}CO(1-0)}{C^{18}O(1-0)}$	$\frac{^{13}CO(1-0)}{C^{18}O(1-0)}$
A	16±6	>28	>1.8
B	7.1±1	13±3	1.9±0.4
C	14±5	12±5	~0.9
D	8.6±3	6.7±2	~0.8
E1	10±2	21±3	2.1±0.3
E2	12±2	59±12	5.0±1
F	15±2	32±7	2.1±0.5
G	15±2	>170	>11
H	21±13	>21	>1
ARM	57±25	>75	>1

Table 6. Column Densities in NGC 6946<sup>a</sup>

GMC	$X_{co}N_{H_2}$ ( $10^{22}cm^{-2}$ )	$^{13}N_{H_2}$ <sup>b</sup> ( $10^{22}cm^{-2}$ )	$^{18}N_{H_2}$ <sup>c</sup> ( $10^{22}cm^{-2}$ )	$VN_{H_2}$ <sup>d</sup> ( $10^{22}cm^{-2}$ )	$\frac{MW X_{CO}}{^{13}X_{co}}$	$\frac{MW X_{CO}}{^{18}X_{co}}$
A	2.0±0.3	0.31±0.1	<0.37	6.8	6.7±2	>5.4
B	2.4±0.3	0.83±0.1	0.96±0.2	...	2.9±0.5	2.5±0.7
C	1.7±0.3	0.31±0.1	0.72±0.2	<4.0	5.5±2	2.4±0.7
D	1.5±0.3	0.41±0.1	1.1±0.2	3.1	3.7±1	1.4±0.3
E1	13±1.3	3.1±0.3	3.2±0.2	...	4.2±0.7	4.1±0.7
E2	12±1.2	2.4±0.3	1.0±0.2	...	5.0±0.8	12±3
F	6.0±0.6	0.98±0.1	0.96±0.2	...	6.1±1	6.3±1
G	6.0±0.6	0.98±0.1	<0.37	6.6	6.1±1	>16
H	1.5±0.3	0.17±0.1	<0.37	1.6	8.8±5	>4.1
ARM <sup>e</sup>	5.4±0.5	0.22±0.1	<0.37	...	25±10	>15

<sup>a</sup>None of the column densities have not been corrected for resolved-out flux. To account for this  $^{13}N_{H_2}$  (and presumably the  $^{18}N_{H_2}$ ) should be divided by  $\sim 0.63$  and  $X_{co}N_{H_2}$  should be divided by  $\sim 0.76$ . Uncertainties reflect only the statistical uncertainties and not the potentially larger systematic uncertainties associated correct abundance ratio and  $T_{ex}$  (see text). Upper Limits are  $2\sigma$ .

<sup>b</sup>Based on the LTE assumption with  $T_{ex} = 20$  K, and  $[^{12}CO/^{13}CO] = 40$ .

<sup>c</sup>Based on the LTE assumption with  $T_{ex} = 10$  K, and  $[^{12}CO/C^{18}O] = 150$ .

<sup>d</sup>Based on the virial masses derived for the isolated GMCs (Table 4).

<sup>e</sup>Based on the position for 'ARM' given in Table 3.